JOURNAL OF GEOPHYSICAL RESEARCH, VOL. 97, NO. B5, PAGES 6779–6797, MAY 10, 1992

Petrology and Magma Chamber Processes at the East Pacific Rise ~ 9°30'N

RODEY BATIZA AND YAOLING NIU

School of Ocean and Earth Science and Technology, University of Hawaii, Honolulu

We present new major and trace element data for a set of closely spaced (< 1.8 km) dredges along a well-studied portion of the East Pacific Rise (EPR) axis near 9°30'N (9°17'N to 9°51'N). With the exception of enriched mid-ocean ridge basalt (E-MORB) at 9°35'N, the lavas are all normal mid-ocean ridge basalt (N-MORB) with a limited range of MgO (8.40-6.22 wt %). Major element and trace element data favor derivation of the melts from a single parental composition by low pressure crystallization of olivine, plagioclase and clinopyroxene in the ratio of 16:62:22. This model is consistent with liquid line of descent models but inconsistent with petrographic observations in that most of the N-MORB lavas have only plagioclase phenocrysts. We ascribe this to gravitational crystal settling of mafic phases and flotation of plagioclase, supported by crystal size distribution data and density relations. Most likely this occurred in the axial magma chamber (AMC) that underlies the EPR in this area. The chemistry of axial lavas varies along axis and correlates roughly with elevation of the axis and depth to the AMC. We interpret these correlations as favoring an AMC that is chemically zoned along-axis, with Fe-rich melts at its distal ends. This favors a central injection of MgO-rich melt with lateral along-axis shallow transport. The height of eruptions along axis is apparently controlled by magma density such that least dense MgO-rich melts build local volcanic constructs of the highest elevation. The E-MORB lavas are older than the N-MORB and probably erupted at a time when the AMC was absent or was much smaller in size than presently. E-MORB could have originated by deep melting processes or very shallow contamination of N-MORB. Its presence in the 9°30'N area supports the notion that magma chambers are not truly steady state. Instead they probably come and go on a time scale of 3000-6000 years. A single parental magma seems to supply melts to the AMC along the entire 60 km segment of the EPR, suggesting that central supply injection sites are widely spaced. Based on our data, there is no evidence for petrologic segmentation corresponding to 4th-order tectonic segmentation in this area; however, it may be present below the resolution of our sampling.

Introduction

Magmatic processes that occur below active mid-ocean ridges are instrumental in building the oceanic crust. Melting is thought to occur as a result of decompression of hot mantle material which rises passively in response to plate separation, with or without additional buoyancy. Recent comparisons of gravity data from fast and slow spreading ridges indicate that fast ridges may be fed mostly by a quasi two-dimensional passive upwelling whereas more complex, three-dimensional buoyant mantle upwelling may be characteristic of slow ridges [*Lin and Phipps Morgan*, 1992]. Another difference between fast and slow ridges appears to be the size and longevity of crustal level magma bodies [*Natland*, 1980*b*]. *Detrick et al.* [1990] report the absence of magma reflectors beneath a magmatically robust section of the mid-Atlantic ridge, whereas at the East Pacific Rise (EPR), there is abundant evidence for present-day magma chamber [e.g., *Sinton and Detrick*, 1992].

The purpose of this paper is to present new petrologic data for a well-studied portion of the EPR at ~ 9°30'N. The samples we studied are from axial dredges spaced ~ 1.8 km apart between 9°17'N and 9°40'N. These new data, together with previous data on samples from 9°40' to 9°51'N, bear on the questions of magma chamber processes and shallow magma supply dynamics at fast ridges. After discussing previous studies of this segment of the EPR, we present and interpret the new petrologic results and discuss their implications.

Paper number 92JB00172.
0148-0227/92/92JB-00172$05.00

Previous Work in the ~ 9°30'N Area of the EPR

The EPR in the vicinity of 9°30'N is one of the best studied segments of the EPR. The rise axis and its flanks have been well mapped using Seabeam and Seamarc II [*Macdonald et al.*, 1984; *Lonsdale*, 1985]. These data, together with other geophysical data and observations provide constraints on the tectonic history and processes of the EPR axis and its offsets [*Macdonald et al.*, 1987, 1988; *Carbotte and Macdonald*, 1992]. The importance of crustal magma bodies and segmentation has been highlighted by a number of seismic studies [e.g. *Detrick et al.*, 1987; *Harding et al.*, 1989; *Kent et al.*, 1991; *Toomey et al.*, 1990; *Mutter et al.*, 1988]. *Haymon et al.* [1991*a*] conducted detailed geologic studies of the axis and mapped the distribution of hydrothermal activity. Follow-up submersible studies [*Haymon et al.*, 1991*b*; *Perfit et al.*, 1991] have provided information on volcanic processes at the axis, and new analyses of samples from the EPR axis and off-axis flanks. Additional basalt samples from the area were collected by *Langmuir et al.* [1986] as part of a larger study of the EPR axis. Nearby seamounts also have been studied in detail [*Fornari et al.*, 1984, 1988; *Allan et al.*, 1989; *Batiza et al.*, 1990].

This segment of the EPR spreads nearly symmetrically at 111 mm yr^{-1} [*Carbotte and Macdonald*, 1992] and is broadly similar to other portions of the EPR nearby, such as the EPR between 10°N and 13°N [e.g. *Macdonald and Fox*, 1988; *Hekinian et al.*, 1989; *Gente et al.*, 1986; *Thompson et al.*, 1989; *Detrick et al.*, 1987; *Perram and Macdonald*, 1990] and the faster spreading southern EPR [*Lonsdale*, 1989; *Sinton et al.*, 1991]. The 9°30'N area contrasts with the 13°N area in that morphologically (broader, higher axis) it appears to have a

more robust magma supply and has a narrower and less deep linear submit collapse [Haymon et al., 1991*a*]. The axial magma chamber (AMC) in the 9°30'N area is continuously present along axis (or nearly so), but varies slightly in depth along axis (Figure 1). South of 9°17'N, the AMC reflector is displaced to the west. Interestingly, in the seismic tomography area (9°27'N to 9°36'N), the region of the lowest velocity about 1-3 km beneath the seafloor is also offset about 1 km to the west of the axis [*Toomey et al.*, 1990] even though the AMC reflector is centered at the axis. In this area,

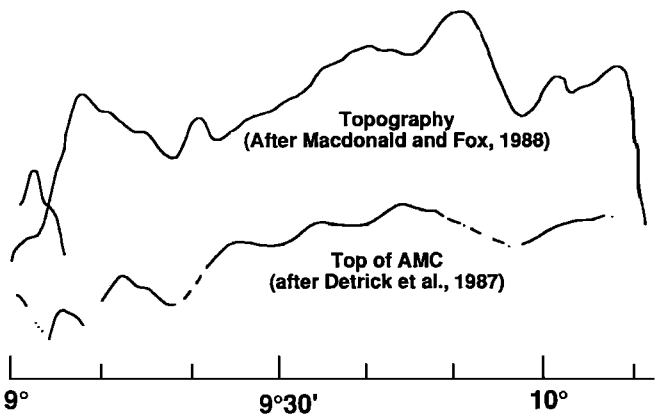

Fig. 1. Along-axis changes in axial topography and depth to the axial magma chamber (AMC) from Detrick et al. [1987] and Macdonald and Fox [1988]. Both profiles are greatly exaggerated vertically to show the rough correlation that exists between topography and depth to the AMC. As shown later, lava chemistry also correlates with these curves. The ranges of depth variation are different for each curve. Axial depth varies from ~ 2700 m to ~ 2540 m (~ 160 m), whereas the top of the AMC varies from ~ 2100 m to ~ 1500 m (sub-bottom). We note that Kent et al. [1991] suggest that depth variations in the AMC may be partly artifactual.

morphologic segmentation (devals at 9°28'N and 9°35'N) corresponds to segmentation in crustal velocity structure, leading *Toomey et al.* [1990] to suggest that small-scale segmentation of the EPR is magmatically controlled. *Toomey et al.* [1990] identify morphologic segmentation of linear EPR volcanoes [*Lonsdale*, 1985] on a scale of 5-10 km along axis. This corresponds to the so-called 4th-order segmentation of *Macdonald et al.* [1988]. Between 9°17'N and 9°55'N, 12 4th-order segment boundaries have been identified (9°17'N, 20', 25', 26.1', 28', 32.7' 35', 37.1', 45', 49', 51.5', and 54'N [*Langmuir et al.*, 1986; *Brodholdt and Batiza*, 1988; *Toomey et al.*, 1990; *Haymon et al.*, 1991*a*] for an average segment length of 5-6 km.

In contrast with the 4th-order volcano-tectonic segmentation, petrologic segmentation of the EPR [*Langmuir et al.*, 1986; *Thompson et al.*, 1989; *Sinton et al.*, 1991*a*] has usually been thought of as occurring on a slightly longer length scale. Indeed, in this paper we show that petrologically, the EPR between 9°20'N and 9°54'N (~ 63 km) is petrologically rather uniform. With the exception of an enriched mid-ocean ridge basalt (E-MORB) at 9°35.7'N, all the axial lavas are N-MORB and appear to be related to a single parental composition. Further, magma temperature or MgO content varies regularly along axis and is crudely correlated with topographic variation. These observations provide clues about shallow processes of magma transport, storage and eruption discussed later.

RESULTS

Dredges

Table 1 lists our sample locations, which are also shown on Figure 2. In most cases, the samples are located near or within the axial summit caldera (ASC) mapped by *Haymon et al.*

TABLE 1. Dredge Locations

Dredge	Start		End		Fix	Depth	Amount
	Latitude	Longitude	Latitude	Longitude	Type*	m	of Rock
R34†	9°16.90'N	104°13.70'W	9°16.75'N	104°13.33'W	1	2611-2615	50 Kg
R35	9°18.71'N	104°13.15'W	9°19.23'N	104°13.34'W	1	2581-2593	15 Kg
R36	9°19.76'N	104°13.09'W	9°19.77'N	104°13.42'W	1	2594-2595	0.5 Kg
R37	9°19.97'N	104°12.88'W	9°20.18'N	104°12.73'W	1	2600-2590	150 Kg
R38	9°20.54'N	104°12.95'W	9°20.81'N	104°12.82'W	2	2597-2609	1 Kg
R39	9°21.19'N	104°12.87'W	9°21.40'N	104°12.76'W	2	2586-2589	250 Kg
R40	9°21.97'N	104°12.83'W	9°22.17'N	104°12.73'W	2	2590-2596	1 Kg
R41	9°24.24'N	104°13.02'W	9°24.08'N	104°13.10'W	2	2598	5 Kg
R42	9°25.05'N	104°13.47'W	9°25.43'N	104°13.46'W	2	2588-2584	20 Kg
R43	9°26.00'N	104°13.68'W	9°26.14'N	104°13.62'W	2	2590	10 g
R44	9°27.96'N	104°14.21'W	9°28.16'N	104°14.15'W	1	2580-2583	20 Kg
R45	9°28.96'N	104°14.31'W	9°29.23'N	104°14.40'W	1	2580-2582	1 g
R46	9°29.99'N	104°14.34'W	9°30.30'N	104°14.30'W	1	2580-2581	20 Kg
R47	9°30.88'N	104°14.46'W	9°31.10'N	104°14.39'W	2	2586-2579	10 Kg
R48	9°32.00'N	104°14.61'W	9°32.15'N	104°14.58'W	2	2579-2573	20 Kg
R49†	9°31.42'N	104°12.37'W	9°31.70'N	104°12.96'W	2	2571-2699	60 Kg
R50†	9°33.23'N	104°14.49'W	9°33.42'N	104°14.42'W	2	2600-2570	10 Kg
R51	9°32.97'N	104°14.69'W	9°33.19'N	104°14.69'W	2	2575-2576	100 Kg
R52	9°33.60'N	104°14.82'W	9°33.81'N	104°14.80'W	1	2590	15 Kg
R53	9°34.38'N	104°14.70'W	9°34.57'N	104°14.68'W	1	2563-2577	10 Kg
R54	9°35.66'N	104°15.05'W	9°35.85'N	104°15.04'W	1	2559-2562	20 Kg
R55	9°36.84'N	104°15.26'W	9°37.05'N	104°15.33'W	1	2565-2565	20 Kg
R56	9°37.84'N	104°15.13'W	9°38.06'N	104°15.05'W	1	2561-2558	0.5 Kg
R57	9°38.89'N	104°15.37'W	9°38.71'N	104°15.40'W	2	2555-2554	10 Kg
R58	9°39.55'N	104°15.51'W	9°39.77'N	104°15.50'W	2	2552-2550	20 Kg
R59	9°40.30'N	104°16.00'W	9°40.50'N	104°16.00'W	2	2552	1 Kg

* Fix types are 1, Global positioning system (GPS) plus Seabeam topography; and 2, transit satellite and Dead-reckoning (DR) plus Seabeam topography.

† denotes off-axis dredges.

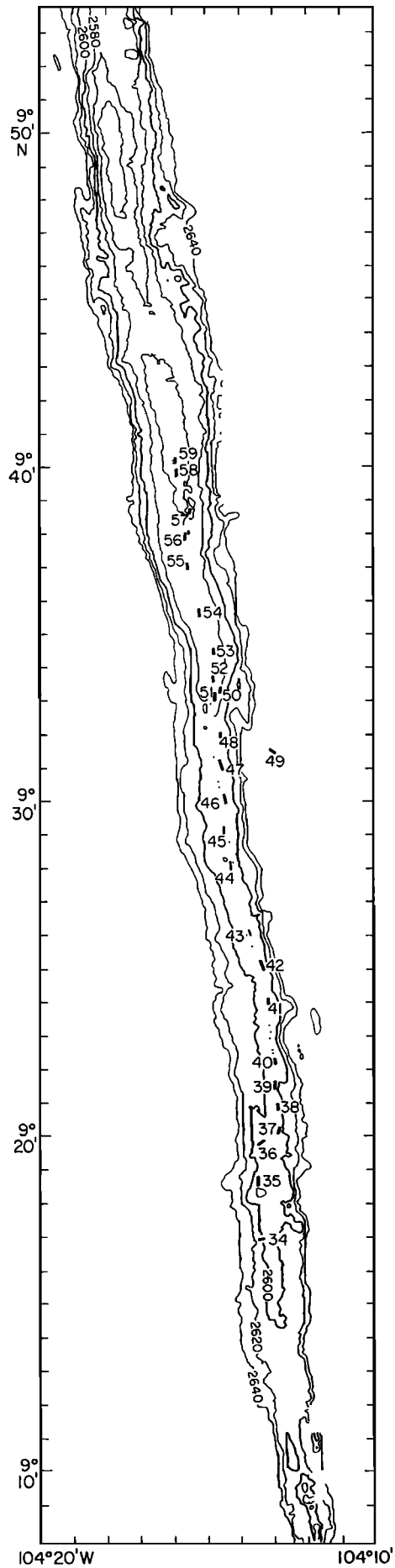

Fig. 2. Map of dredge locations. The Sea Beam base map is from *Toomey et al.* [1990], and the dredge locations are from Table 1. The dotted line shows the approximate position of the axial summit caldera (ASC) from *Haymon et al.* [1991*a*]. Note that most of the new dredges are near the ASC.

[1991*a*] and are thus less than a few thousand years old. More recent sampling of the area by submersible and transponder-navigated rock cores [*Perfit et al.*, 1991] greatly extends sampling of this part of the EPR. The dredges, collected on the R/V Thomas Washington in February 1988 (RAITT 02), were primarily navigated using Seabeam and the new Seabeam map of *Toomey et al.* [1990]. The beam profile of Seabeam was used to track the ASC along axis. The dredges consistently were done with zero wire angle, 5-10 min on the bottom and took an average of 2.5 hours each.

All of the samples recovered are extremely fresh and glassy, with the exception of those in dredges 34, 49, and 50 located off axis (Figure 2). Fresh glass was also obtained in the off-axis dredges, however the rocks are generally duller and appear older than the freshest samples. Average dredge spacing of the new dredges between 9°17'N and 9°40'N is ~ 1.8 km. In this study we also use results obtained by *Langmuir et al.* [1986] from the CHEPR expedition. Dredge locations and chemical analyses for dredges CH-84, CH-91 between 9°19'N and 9°49.2'N are given in the Joint Oceanographic Institutions (JOI) synthesis of EPR data [*Tighe*, 1988]. In addition, we use data from samples collected by ALVIN dive 1567 at the EPR ~ 9°51'N [*Fornari et al.*, 1988; *Allan et al.*, 1989]. Most of the samples collected and analyzed are fragments of lobate pillows and associated ponded/collapse deposits and more rarely true sheet flows and pillow buds.

Petrography

All the samples between 9°17'N and 9°51'N are sparsely phyric with at most a few percent phenocrysts and microphenocrysts. A major petrographic break occurs at about 9°20'N to 9°21'N, roughly coincident with the shift in location of the AMC relative to the axis [*Mutter et al.*, 1988]. South of 9°21'N, where the AMC is centered off-axis to the west, the lavas have more abundant phenocrysts and corroded megacrysts of olivine, plagioclase, and clinopyroxene (up to 7% total). In contrast, north of this boundary up to the Clipperton transform, the EPR axis lavas are more sparsely phyric (< 3%) and contain almost exclusively plagioclase phenocrysts and micro phenocrysts. Many also contain microlites and tiny (up to 60 μm, most < 30 μm) skeletal microphenocrysts of olivine. Between 9°21N and 9°25'N the lavas contain both sparse plagioclase and olivine phenocrysts. The olivine phenocrysts are up to 200 μm long but are greatly subordinate to plagioclase up to 3 mm in length. A single sample (R41-2) contains cpx crystals in glass. These are anhedral to subhedral, exhibit sector zoning and do not resemble typical phenocrysts. Instead, they resemble cpx grains which commonly occur in the more crystalline portions of the lavas as glomerophyric clusters with plagioclase.

Overall, the samples exhibit mineralogic and textural features typical of EPR N-MORB elsewhere along the axis [e.g., *Batiza et al.*, 1977; *Natland*, 1980*a*]. One exception is the absence of spinel commonly found in high-MgO EPR lavas [*Natland*, 1989]. Another is the paucity of vesicles decorated

TABLE 2. Representative Probe Microanalyses of Olivine

	R39-8	R49-3	R49-4	R50-1	R50-4	R50-7	R52-1	R56-6	R57-5	R57-6	R52-6	CH90-2
N	12	11	10	7	10	9	9	9	10	5	17	10
SiO_2	39.72	39.30	39.42	40.03	39.94	40.06	39.82	39.74	39.84	40.26	39.64	41.73
FeO	14.71	14.39	14.35	10.91	11.27	11.92	14.68	12.49	13.51	12.90	14.94	15.63
MnO	0.23	0.22	0.24	0.17	0.11	0.21	0.24	0.22	0.23	0.19	0.00	0.26
MgO	45.40	44.18	44.65	47.07	47.55	46.51	44.60	46.43	46.03	45.68	43.32	42.76
CaO	0.39	0.37	0.34	0.37	0.39	0.35	0.34	0.35	0.37	0.52	0.38	0.34
NiO	0.11	0.08	0.20	0.30	0.17	0.23	0.12	0.18	0.16	0.22	0.12	0.11
Total	100.56	98.54	99.20	98.85	99.43	99.28	99.80	99.41	100.14	99.77	98.40	100.83
Si	0.993	1.001	0.998	1.000	0.994	1.001	1.002	0.995	0.995	1.005	1.011	1.038
Fe^{2+}	0.307	0.306	0.303	0.228	0.234	0.249	0.308	0.261	0.282	0.269	0.318	0.324
Mn	0.005	0.005	0.005	0.004	0.002	0.004	0.005	0.005	0.005	0.004	0.000	0.005
Mg	1.690	1.676	1.683	1.752	1.762	1.731	1.671	1.732	1.712	1.699	1.646	1.584
Ca	0.010	0.010	0.009	0.010	0.010	0.009	0.009	0.009	0.010	0.014	0.010	0.009
Ni	0.002	0.002	0.004	0.006	0.003	0.005	0.002	0.004	0.003	0.004	0.002	0.002
Sum	3.007	2.999	3.002	3.000	3.006	2.999	2.998	3.005	3.005	2.995	2.989	2.962
Fo	0.839	0.839	0.840	0.876	0.876	0.866	0.837	0.861	0.851	0.854	0.833	0.823
Fa	0.152	0.153	0.151	0.114	0.116	0.124	0.154	0.130	0.140	0.135	0.161	0.169
Ca-Ol	0.005	0.005	0.005	0.005	0.005	0.005	0.005	0.005	0.005	0.007	0.005	0.005
Ni-Ol	0.001	0.001	0.002	0.003	0.002	0.002	0.001	0.002	0.002	0.002	0.001	0.001
Mn-Ol	0.002	0.002	0.003	0.002	0.001	0.002	0.003	0.002	0.002	0.002	0.000	0.003

N is number of analyses. Analyses were done at the University of Hawaii, Honolulu.

with sulfide blebs. Sulfide minerals are present, but occur only as subspherical blebs up to 100 μm in diameter; the walls of tiny vesicles are free of sulfides.

Olivine microphenocrysts and microlites are virtually unzoned (Table 2) and exhibit a narrow range of chemical variations (Fo_{88} to Fo_{82}). Figure 3 shows that the olivine is apparently in equilibrium with its host melt [e.g., *Roeder and Emslie*, 1970; *Ulmer*, 1989] confirming inferences based on olivine morphology. Plagioclase crystals vary more widely in chemistry (Figure 4 and Table 3) from An_{85} to An_{55}. Groundmass plagioclase microlites are systematically more sodic than phenocrysts and microphenocrysts which show a narrower range of variation (most are An_{70} to An_{82}: Figure 4). Zoning patterns in plagioclase phenocrysts are, as usual, very complex, with both normal and reverse zoning observed within a single rock. Despite complex zoning and compositional variation of phenocryst cores (Figure 5) within single rocks, the plagioclase phenocrysts are euhedral and appear to be in equilibrium. This cannot be confirmed, as plagioclase-melt equilibria is not yet fully worked out and is strongly dependent on the bulk composition of melt and other variables [e.g., *Glazner*, 1984; *Housh and Luhr*, 1991].

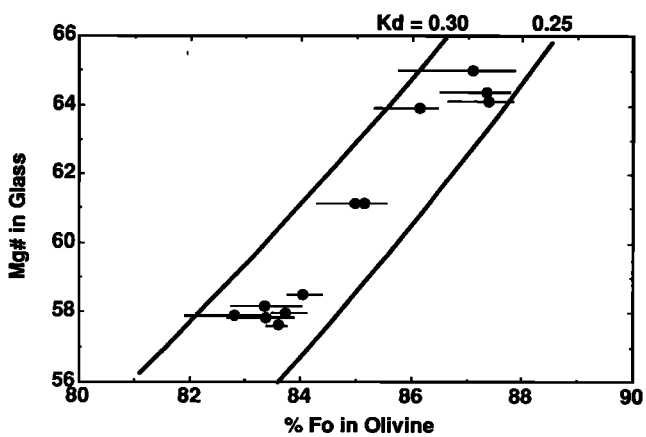

Fig. 3. Olivine analyses plotted against the Mg/(Mg+Fe^{2+}) of host glass. For reference, we show K_d (Fe-$Mg^{Ol\text{-}Liq}$) values of 0.25 and 0.30 calculated using the method of *Roeder and Emslie* [1970]. The dots are mean compositions, and the lines show observed range of variation. Note that most olivines are in equilibrium with their host melt.

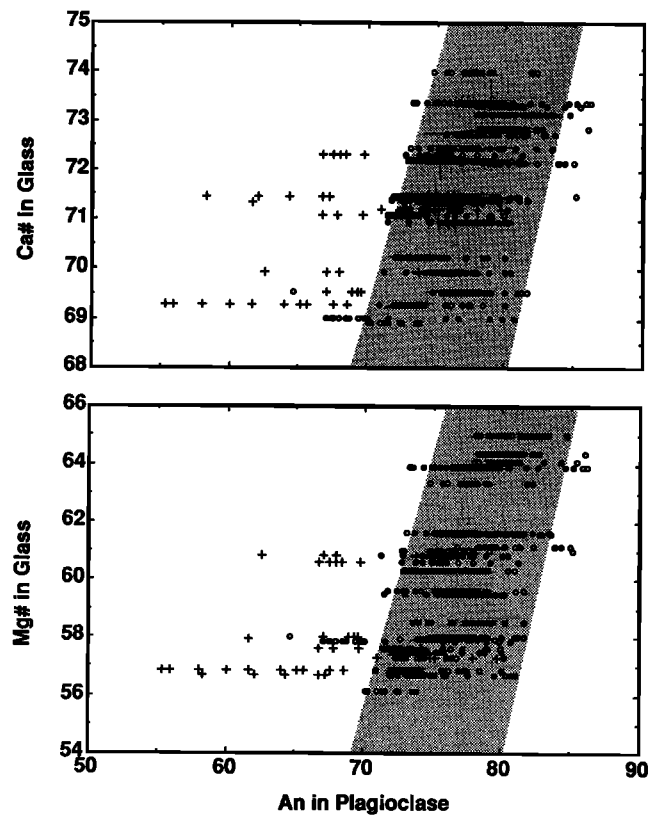

Fig. 4. Plagioclase analyses plotted against Ca/(Ca+Na) and Mg/(Mg+Fe^{2+}) of their host glass. Solid circles are cores and open circles rims of phenocrysts and microphenocrysts; crosses are microlites. The shaded area is a field for analyses of crystals that appear textually to be in equilibrium with their host melt.

TABLE 3. Representative Probe Microanalyses of Plagioclase

	R39-1	R39-1	R40-5	R40-5	R41-1	R42-1	R42-1	R46-2	R46-9	R46-9	R47-1	R47-1	R48-1
N	15	9	6	4	10	28	17	5	16	8	17	8	1
Grain	c	r	c	r	g	c	r	g	c	r	c	r	g
SiO_2	49.25	48.86	50.26	50.27	52.65	49.48	49.43	52.34	49.21	49.45	48.14	48.51	52.06
Al_2O_3	32.19	32.54	31.54	31.58	29.57	32.16	32.37	29.04	32.20	31.94	32.89	32.77	29.27
FeOt	0.45	0.45	0.54	0.60	0.93	0.42	0.45	1.07	0.50	0.51	0.37	0.41	0.84
MgO	0.21	0.19	0.21	0.21	0.28	0.22	0.23	0.39	0.21	0.21	0.22	0.20	0.35
CaO	15.41	15.74	14.39	14.58	12.84	15.41	15.51	12.67	15.28	15.10	15.90	15.62	12.14
Na_2O	2.65	2.49	3.09	3.10	4.29	2.73	2.66	3.95	2.75	2.92	2.24	2.36	4.14
K_2O	0.02	0.02	0.02	0.02	0.04	0.02	0.02	0.05	0.02	0.03	0.02	0.02	0.06
Total	100.17	100.29	100.03	100.34	100.60	100.46	100.67	99.51	100.17	100.15	99.78	99.89	98.86
Si	2.249	2.232	2.292	2.288	2.384	2.253	2.247	2.394	2.248	2.259	2.210	2.223	2.392
Al	1.733	1.750	1.694	1.693	1.577	1.726	1.734	1.565	1.734	1.720	1.779	1.769	1.584
Fe^{3+}	0.018	0.018	0.014	0.019	0.039	0.021	0.019	0.041	0.018	0.021	0.011	0.008	0.024
Ca	0.754	0.770	0.703	0.711	0.623	0.752	0.755	0.621	0.748	0.739	0.782	0.766	0.597
Fe^{2+}	0.002	0.002	0.007	0.005	0.002	0.001	0.002	0.004	0.003	0.001	0.004	0.007	0.009
Mg	0.014	0.013	0.014	0.014	0.019	0.015	0.015	0.026	0.015	0.015	0.015	0.014	0.024
Na	0.234	0.221	0.273	0.273	0.376	0.241	0.234	0.350	0.244	0.258	0.200	0.209	0.369
K	0.001	0.001	0.001	0.001	0.002	0.001	0.001	0.003	0.001	0.002	0.001	0.001	0.004
Cations	5.005	5.007	4.998	5.003	5.022	5.011	5.007	5.004	5.010	5.014	5.002	4.998	5.002
An%	76.20	77.62	71.98	72.19	62.16	75.61	76.24	63.75	75.35	73.98	79.58	78.46	61.62
Or%	0.11	0.11	0.09	0.09	0.25	0.12	0.13	0.28	0.10	0.15	0.11	0.13	0.36

	R49-4	R49-4	R49-4	R50-7	R52-1	R54-2	R54-2	R54-2	R56-6	R56-6	R56-7	R56-7	R58-1
N	15	10	4	15	4	15	10	5	9	7	14	8	5
Grain	c	r	g	c	g	c	r	g	c	r	c	r	g
SiO_2	48.68	48.65	50.71	47.94	49.87	48.52	48.64	50.69	48.64	48.62	48.47	48.24	51.17
Al_2O_3	32.39	32.51	30.62	32.89	31.08	32.49	32.59	30.55	32.40	32.45	32.73	32.86	29.92
FeOt	0.55	0.61	0.72	0.41	0.8	0.52	0.54	0.93	0.39	0.40	0.41	0.44	0.75
MgO	0.20	0.19	0.27	0.22	0.29	0.21	0.19	0.35	0.25	0.25	0.21	0.24	0.43
CaO	15.53	15.56	13.80	16.06	13.99	15.37	15.47	13.65	15.63	15.71	15.79	15.92	13.83
Na_2O	2.52	2.49	3.45	2.24	3.35	2.63	2.61	3.51	2.55	2.46	2.44	2.35	3.56
K_2O	0.02	0.03	0.04	0.02	0.04	0.06	0.05	0.09	0.02	0.01	0.02	0.02	0.03
Total	99.90	100.04	99.61	99.77	99.41	99.79	100.09	99.78	99.88	99.91	100.07	100.06	99.69
Si	2.232	2.229	2.322	2.204	2.293	2.227	2.227	2.320	2.230	2.229	2.219	2.210	2.342
Al	1.751	1.754	1.653	1.781	1.683	1.758	1.758	1.649	1.751	1.753	1.766	1.774	1.614
Fe^{3+}	0.017	0.017	0.025	0.015	0.024	0.015	0.015	0.031	0.019	0.018	0.015	0.016	0.044
Ca	0.763	0.764	0.677	0.790	0.688	0.756	0.756	0.669	0.767	0.771	0.774	0.781	0.678
Fe^{2+}	0.004	0.007	0.005	0.002	0.007	0.005	0.006	0.004	0.001	0.001	0.003	0.004	0.004
Mg	0.014	0.013	0.018	0.015	0.020	0.014	0.013	0.024	0.017	0.017	0.015	0.016	0.029
Na	0.224	0.221	0.306	0.199	0.298	0.234	0.231	0.311	0.226	0.219	0.216	0.209	0.316
K	0.001	0.002	0.002	0.001	0.002	0.003	0.003	0.005	0.001	0.001	0.001	0.001	0.002
Cations	5.006	5.005	5.008	5.007	5.016	5.013	5.012	5.014	5.013	5.009	5.010	5.010	5.026
An%	77.19	77.44	68.72	79.80	69.63	76.09	76.36	67.88	77.15	77.85	78.10	78.84	68.08
Or%	0.15	0.17	0.24	0.10	0.21	0.34	0.31	0.54	0.09	0.07	0.09	0.09	0.20

N is number of analyses; grain is c, core; r, rim; and g, groundmass. Fe^{3+} is obtained by stoichiometry and charge balance. Note the absence of systematic zoning. Analyses were done at the University of Hawaii, Honolulu.

The size distribution of plagioclase phenocrysts and microphenocrysts in the samples is interesting (Figure 6). We employ the crystal size distribution (CSD) technique of *Marsh* [1988] and *Cashman and Marsh* [1988], but to get adequate statistics, multiple thin sections had to be counted. A typical EPR basalt from the 9°30'N area contains only 4-60 plagioclase crystals over 50 μm in size per thin section. We counted five thin sections each for two relatively primitive (CH-91and ALVIN 1567) and two relatively evolved (R40 and CH-85) lavas and combined the data. Even so, statistics are still rather poor with totals of only 117, 41, 68, and 160 crystals for each of the four rocks. Despite the low counts, the patterns of Figure 6 are reasonably consistent, with values of $\ln(N)$ (where N is crystals per cm^3) showing a log normal distribution with crystal size up to crystal sizes of ~ 0.5 mm. Such a log-normal distribution is expected for simple cases of closed system crystallization. In contrast, the almost flat distribution of large crystals in the EPR lavas is unusual. One

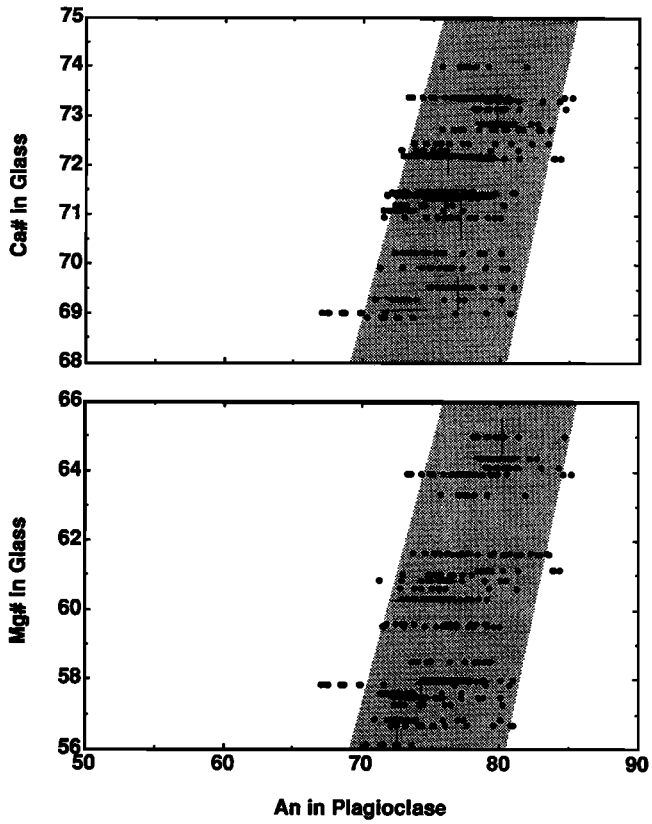

Fig. 5. Same as Figure 4 except that only the cores of plagioclase phenocrysts are plotted.

explanation is that the original log-normal CSD patterns have been altered by a gain of large-sized plagioclase crystals (see *Marsh* [1988] for additional discussion).

Basalt Glass Chemistry

With one exception (E-MORB glasses in dredge R54), all the samples between 9°17'N and 9°51'N are normal MORB (N-MORB) with a limited range of MgO (8.4 to 6.22 wt %; Table 4). We analyzed basaltic glasses using electron microprobes at the University of Hawaii, Honolulu and the Smithsonian Institution, Washington, D. C. (T. O'Hearn, analyst). In order to compare all these data, plus data from the Lamont-Doherty probe for CHEPR samples, we conducted a limited interlaboratory comparison in which each laboratory analyzed glasses from 16 different MORB samples. Small systematic differences exist among all probe laboratories, but these can be corrected. The data of Table 4*a* have been adjusted using the factors given in Table 4*b*. Accuracy and precision of the University of Hawaii electron microprobe for basalt glasses and minerals are given by *Garcia and Wolfe* [1988] and *Garcia et al.* [1986].

Except for the E-MORB samples, the samples display chemical variations of the type typical of N-MORB suites from elsewhere along the mid-ocean ridge system [e.g. *Perfit et al.*, 1983; *Thompson et al.*, 1989; *Walker et al.*, 1979] often interpreted as the result of shallow fractionation processes. The 9°30'N suite is quite coherent (with scatter) and comprises a linear, continuous series on MgO variation diagrams (Figure 7). For convenience in data handling, we have computed group means (see Table 4 notes) and plot these group means in Figure 8 (MgO variation diagrams) and Figure 9 (normative mineralogy).

Trace element data by instrumentation neutron activation analysis (INAA) for selected glasses are given in Table 5. These also show limited variation which can be explained almost entirely by fractional crystallization as discussed later.

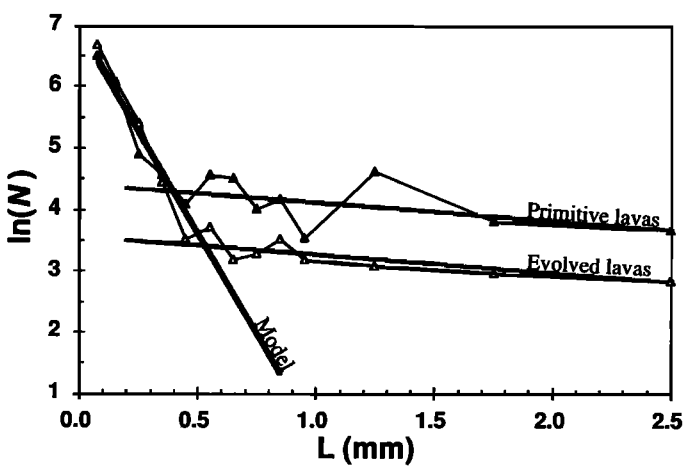

Fig. 6. Crystal size distribution (CSD) data for relatively primitive and relatively evolved lavas from the 9°30'N area. The ln(N) is the natural logarithm of the number of crystals per cubic centimeter, and L is the length (in milimeters) of plagioclase crystals. See text for discussion and details. These CSD patterns, which deviate from log normal at large crystal sizes, provide evidence that plagioclase crystals were added to the magma.

Along-Axis Chemical Variation

The chemical variation of lavas along axis in the 9°30'N area is not random. While there is significant chemical variation at each place along the axis, the mean values exhibit a fairly regular pattern of along-axis variation. Figure 10 shows that MgO and TiO_2 (other element as well) show local scatter, but also a crude variation along axis that correlates with topography. The along-axis pattern is clearly evident after smoothing with a moving boxcar filter (Figure 11). Local topographic highs at 9°48'N, and the 9°32'N to 9°38'N area correspond to the highest MgO and lowest TiO_2 values. The mean and maximum MgO values decrease away from the local topographic highs. Local topographic lows (e.g., at 9°43'N) and topographic gradients in slope (e.g., the deepening between 9°38'N and 9°20'N) can also be seen in the pattern of along-axis chemical variation. At the same time, there is a range of variation at any latitude, for example MgO shows a variation of 1 wt % or more throughout the 9°30'N area. However, smoothing of this scatter shows that axial topography and depth to the top of the AMC (Figure 1) are correlated with axial MORB chemistry. As expected, computed melt density [*Niu and Batiza*, 1991*a*] and melt eruption temperature [*Bender et al.*, 1984] shown in Figure 12 also exhibit a crude correlation with depth to the AMC and axial topography, with the least dense, hottest magmas erupting at the local topographic highs near 9°36'N and 9°48'N to 9°50'N.

Radiogenic Isotopes and Eruption Ages

Harpp et al. [1990] presented Sr and Nd isotope data for samples from the 9°30'N area. These results will be fully presented elsewhere; however, we note here that the N-MORB samples exhibit only a small range of $^{87}Sr/^{86}Sr$ (0.70248 to

TABLE 4*a*. Major Element Chemistry of EPR Basaltic Glasses

	R37-1	R37-2	R37-3	R37-4	R37-5	R37-6	R37-7	R37-8	R37-12	R38-1	R39-1	R39-2	R39-3	R39-4
SiO_2	50.91	50.80	50.77	50.91	50.48	50.13	50.62	51.14	51.44	51.13	49.98	50.43	50.61	50.32
TiO_2	1.66	1.66	1.64	1.66	1.61	1.65	1.70	1.67	1.68	1.75	1.65	1.59	1.62	1.62
Al_2O_3	14.46	14.50	14.46	14.58	14.44	14.49	14.39	14.64	14.57	14.34	14.75	15.17	15.20	15.15
FeO	10.77	10.64	10.47	10.65	10.73	10.58	10.52	10.71	10.71	10.99	10.01	10.18	10.16	10.06
MnO	0.17	0.21	0.21	0.24	0.21	0.20	0.23	0.19	0.19	na	0.21	0.16	0.18	0.17
MgO	7.14	7.15	7.23	7.14	7.14	7.16	7.16	7.16	7.09	7.05	7.43	7.51	7.33	7.44
CaO	11.64	11.42	11.36	11.48	11.46	11.36	11.14	11.37	11.54	11.50	11.70	11.94	11.99	11.86
Na_2O	2.68	2.71	2.74	2.71	2.74	2.75	2.77	2.75	2.58	2.68	2.64	2.66	2.70	2.68
K_2O	0.10	0.11	0.11	0.12	0.09	0.11	0.10	0.11	0.12	0.14	0.13	0.16	0.14	0.16
P_2O_5	0.15	0.18	0.20	0.14	0.19	0.20	0.14	0.22	0.23	0.20	0.15	0.17	0.17	0.18
Total	99.69	99.39	99.18	99.63	99.08	98.62	98.77	99.97	100.20	99.78	98.65	99.97	100.10	99.63
Mg#	56.77	57.10	57.77	57.04	56.85	57.27	57.41	57.00	56.72	55.96	59.50	59.36	58.84	59.43

	R39-5	R39-6	R39-7	R39-8	R39-9	R39-10	R39-11	R39-12	R39-16	R39-17	R39-18	R39-19	R40-1	R40-2
SiO_2	50.44	49.84	50.21	49.95	50.27	50.56	50.05	50.31	50.31	50.06	50.07	49.46	50.84	50.90
TiO_2	1.62	1.69	1.64	1.58	1.63	1.68	1.66	1.68	1.63	1.67	1.64	1.63	1.86	1.84
Al_2O_3	14.70	15.03	14.98	14.83	15.15	14.76	14.87	14.84	14.96	14.81	14.67	14.92	14.36	14.32
FeO	10.35	10.23	10.04	10.34	10.14	10.42	10.41	10.47	10.42	10.38	10.27	10.09	11.29	10.67
MnO	na	0.17	0.19	na	0.19	0.19	0.16	0.19	na	0.18	0.18	0.17	0.17	0.21
MgO	7.51	7.44	7.33	7.36	7.51	7.33	7.38	7.36	7.40	7.51	7.31	7.47	6.80	6.82
CaO	11.80	11.78	11.77	11.97	11.89	12.01	12.05	11.99	11.82	11.67	11.95	12.04	11.45	11.34
Na_2O	2.67	2.72	2.71	2.64	2.70	2.66	2.63	2.67	2.61	2.65	2.60	2.65	2.79	2.82
K_2O	0.11	0.16	0.14	0.11	0.14	0.12	0.12	0.13	0.12	0.13	0.13	0.12	0.14	0.16
P_2O_5	0.19	0.19	0.20	0.18	0.17	0.17	0.17	0.17	0.18	0.18	0.18	0.17	0.21	0.23
Total	99.39	99.25	99.21	98.96	99.80	99.91	99.50	99.81	99.45	99.26	99.01	98.73	99.91	99.31
Mg#	58.97	59.02	59.12	58.50	59.47	58.22	58.41	58.21	58.45	58.90	58.50	59.46	54.41	55.85

	R40-3	R40-4	R40-5	R41-1	R41-2	R41-3	R41-4	R42-1	R42-2	R42-3	R42-4	R42-5	R42-6	R42-7
SiO_2	50.10	49.95	50.54	50.79	50.59	49.95	50.07	51.04	50.27	50.96	51.14	50.92	51.13	50.88
TiO_2	1.90	1.90	1.88	1.70	1.65	1.77	1.70	1.54	1.49	1.50	1.54	1.52	1.51	1.47
Al_2O_3	14.15	14.28	14.33	14.72	14.61	14.45	14.40	14.75	14.93	14.94	14.95	14.83	14.97	15.06
FeO	11.22	11.27	10.48	10.63	10.40	10.63	10.51	9.98	9.97	9.89	10.00	9.84	9.85	9.87
MnO	0.19	0.20	0.22	0.20	0.21	0.20	0.19	na	0.20	0.18	0.17	0.17	0.18	0.18
MgO	7.01	6.75	6.76	7.07	7.06	7.11	7.22	7.66	7.76	7.75	7.76	7.60	7.78	7.80
CaO	11.76	11.26	11.27	11.75	11.79	11.64	11.60	12.03	11.93	12.12	12.07	11.93	12.06	12.26
Na_2O	2.77	2.76	2.80	2.87	2.80	2.85	2.70	2.55	2.58	2.51	2.57	2.56	2.55	2.63
K_2O	0.13	0.17	0.14	0.13	0.14	0.15	0.13	0.11	0.13	0.12	0.10	0.13	0.11	0.13
P_2O_5	0.25	0.23	0.13	0.21	0.19	0.20	0.23	0.17	0.24	0.16	0.17	0.18	0.15	0.14
Total	99.48	98.76	98.56	100.10	99.43	98.95	98.75	99.83	99.50	100.10	100.50	99.68	100.30	100.40
Mg#	55.31	54.27	56.10	56.84	57.35	56.97	57.65	60.32	60.65	60.81	60.59	60.47	61.00	61.01

	R44-1	R44-2	R44-3	R44-4	R44-5	R44-6	R44-7	R44-12	R44-13	R44-14	R45SG	R46-1	R46-2	R46-3
SiO_2	50.82	50.97	51.35	51.15	51.10	50.88	50.46	51.34	50.95	50.63	50.59	50.40	50.71	50.61
TiO_2	1.71	1.71	1.72	1.70	1.71	1.69	1.66	1.72	1.73	1.74	1.71	1.63	1.71	1.63
Al_2O_3	14.67	14.61	14.55	14.57	14.59	14.47	14.49	14.51	14.59	14.60	14.50	14.47	14.82	14.59
FeO	9.95	10.54	10.58	10.57	10.63	10.61	10.58	10.58	10.66	10.77	10.55	10.31	10.36	10.10
MnO	0.21	0.19	0.19	0.18	0.18	na	na	0.18	0.19	0.19	na	0.21	na	0.18
MgO	7.09	7.30	7.28	7.27	7.26	7.18	7.18	7.31	7.32	7.33	7.35	7.45	6.84	6.87
CaO	11.57	11.85	11.79	11.80	11.91	11.77	11.77	11.80	11.79	11.82	11.76	11.53	12.10	11.57
Na_2O	2.88	2.63	2.63	2.61	2.68	2.62	2.66	2.64	2.69	2.68	2.65	2.65	2.66	2.73
K_2O	0.16	0.11	0.12	0.11	0.12	0.12	0.12	0.11	0.11	0.11	0.14	0.14	0.13	0.16
P_2O_5	0.19	0.20	0.17	0.18	0.19	0.20	0.15	0.19	0.19	0.18	0.16	0.18	0.17	0.19
Total	99.24	100.10	100.40	100.20	100.40	99.54	99.07	100.40	100.20	100.10	99.41	98.98	99.50	98.63
Mg#	58.53	57.85	57.67	57.66	57.49	57.27	57.34	57.77	57.62	57.40	57.98	58.87	56.67	57.40

	R46-4	R46-5	R46-6	R46-7	R46-8	R46-9	R46-10	R47-1	R47-2	R47-3	R47-4	R47-5	R47-6	R48-1
SiO_2	50.59	51.25	50.41	50.64	50.76	50.82	50.70	50.33	50.50	50.65	50.41	50.32	50.67	50.83
TiO_2	1.64	1.68	1.65	1.61	1.68	1.64	1.69	1.43	1.40	1.41	1.40	1.39	1.61	1.70
Al_2O_3	14.64	14.60	14.60	14.62	14.64	14.60	14.53	15.22	15.16	15.30	15.17	15.18	14.60	14.65
FeO	10.24	10.00	10.29	10.26	10.50	10.53	10.51	9.74	9.50	9.71	9.58	9.59	10.40	10.36
MnO	0.19	0.22	0.18	0.22	0.20	0.20	0.18	0.21	0.20	na	0.16	0.18	0.19	0.16
MgO	6.92	7.43	7.40	7.36	7.23	7.18	7.17	7.89	7.88	7.87	7.88	7.82	7.29	7.20
CaO	11.90	11.59	11.57	11.53	11.53	11.61	11.70	12.06	11.83	12.28	11.91	11.88	11.58	11.75
Na_2O	2.60	2.66	2.66	2.71	2.68	2.71	2.65	2.49	2.61	2.57	2.57	2.58	2.67	2.60
K_2O	0.11	0.13	0.13	0.13	0.13	0.13	0.11	0.13	0.13	0.12	0.15	0.14	0.11	0.11
P_2O_5	0.19	0.13	0.17	0.19	0.19	0.19	0.20	0.21	0.17	0.16	0.17	0.15	0.18	0.21
Total	99.02	99.68	99.07	99.27	99.54	99.62	99.44	99.71	99.39	100.10	99.40	99.23	99.29	99.58
Mg#	57.23	59.53	58.75	58.69	57.70	57.47	57.48	61.60	62.16	61.62	61.98	61.76	58.12	57.92

TABLE 4a. (continued)

	R48-2	R48-3	R48-4	R48-5	R48-6	R49-1	R49-2	R49-3	R49-4	R50-1	R50-2	R50-3	R50-4	R50-5
SiO_2	50.67	50.50	50.44	50.55	50.49	50.14	51.02	50.62	50.07	50.24	50.38	50.27	50.29	49.93
TiO_2	1.66	1.62	1.62	1.66	1.66	1.90	1.87	1.69	1.67	1.29	1.26	1.26	1.23	1.25
Al_2O_3	14.50	14.70	14.67	14.59	14.58	14.21	14.17	14.69	15.09	15.69	15.64	15.51	15.61	15.70
FeO	10.47	10.43	10.46	10.42	10.41	11.20	11.31	10.04	10.17	9.22	9.02	9.25	9.16	9.00
MnO	0.18	0.18	na	0.18	0.20	0.22	0.21	0.22	na	0.18	0.16	0.17	0.15	na
MgO	7.23	7.08	7.08	6.95	7.27	6.58	6.22	6.95	7.08	8.31	8.26	8.29	8.35	8.40
CaO	11.53	11.71	11.87	11.66	11.75	11.04	11.25	11.44	11.90	12.21	12.17	12.10	12.13	12.27
Na_2O	2.67	2.70	2.65	2.70	2.69	2.90	2.86	2.83	2.87	2.45	2.47	2.46	2.49	2.43
K_2O	0.13	0.11	0.14	0.12	0.14	0.14	0.14	0.23	0.26	0.10	0.10	0.12	0.11	0.12
P_2O_5	0.19	0.18	0.17	0.22	0.17	0.23	0.19	0.24	0.18	0.16	0.13	0.14	0.14	0.12
Total	99.24	99.23	99.10	99.06	99.36	98.56	99.25	98.94	99.29	99.86	99.59	99.59	99.67	99.22
Mg#	57.75	57.36	57.28	56.91	58.04	53.79	52.13	57.83	57.96	64.09	64.47	63.97	64.35	64.90

	R50-6	R50-7	R51-1	R51-2	R51-3	R51-4	R51-5	R51-6	R51-7	R51-8	R51-9	R51-10	R51-11	R51-12
SiO_2	50.45	50.46	50.32	50.43	50.96	50.96	50.81	51.06	50.91	50.78	50.73	50.74	50.88	50.82
TiO_2	1.28	1.28	1.20	1.27	1.49	1.49	1.49	1.47	1.52	1.46	1.50	1.47	1.52	1.53
Al_2O_3	15.58	15.55	15.73	15.44	14.69	14.68	14.61	14.75	14.67	14.54	14.73	14.72	14.50	14.85
FeO	9.03	8.93	9.17	9.13	9.90	10.12	9.97	10.08	10.14	9.81	10.00	10.07	10.06	10.10
MnO	0.19	0.19	na	0.18	0.20	0.18	0.19	0.21	0.18	0.18	0.21	0.20	0.19	0.18
MgO	8.31	8.37	7.98	7.99	7.37	7.34	7.42	7.33	7.39	7.43	7.48	7.39	7.43	7.22
CaO	12.17	12.21	12.52	12.25	11.89	12.01	11.96	11.79	12.07	11.67	12.01	12.01	12.07	12.19
Na_2O	2.40	2.47	2.52	2.48	2.66	2.65	2.64	2.69	2.70	2.63	2.71	2.66	2.68	2.73
K_2O	0.10	0.11	0.09	0.09	0.11	0.09	0.09	0.09	0.08	0.09	0.10	0.09	0.08	0.07
P_2O_5	0.13	0.11	0.12	0.12	0.14	0.16	0.14	0.16	0.16	0.13	0.15	0.15	0.14	0.15
Total	99.64	99.69	99.65	99.38	99.40	99.70	99.32	99.63	99.83	98.72	99.62	99.49	99.57	99.83
Mg#	64.57	64.98	63.28	63.42	59.59	58.95	59.59	59.03	59.08	60.01	59.71	59.22	59.41	58.59

	R51-13	R51-14	R51-15	R51-16	R52-1	R52-2	R52-3	R52-4	R52-5	R52-6	R53SG	R54-1	R54-2	R54-3
SiO_2	50.86	51.02	50.66	51.04	50.40	50.69	50.48	50.39	50.43	50.55	50.09	50.38	49.83	50.25
TiO_2	1.48	1.55	1.53	1.48	1.69	1.62	1.63	1.67	1.60	1.65	1.23	1.62	1.58	1.64
Al_2O_3	14.63	14.70	14.65	14.68	14.88	14.84	14.97	14.71	14.79	14.54	16.08	15.65	15.93	15.68
FeO	9.84	10.92	10.25	10.07	10.54	10.53	10.53	10.34	10.42	10.29	8.86	9.01	9.19	8.98
MnO	0.21	0.22	na	0.21	na	0.19	0.20	0.19	0.19	0.21	na	0.18	na	0.19
MgO	7.33	6.96	7.49	7.29	7.23	7.34	7.19	7.28	7.22	7.21	8.37	7.37	7.21	7.33
CaO	11.80	11.81	12.03	12.01	11.74	11.75	11.82	11.71	11.54	11.52	12.36	11.66	11.87	11.65
Na_2O	2.67	2.70	2.69	2.67	2.63	2.62	2.67	2.65	2.60	2.69	2.44	2.77	2.81	2.76
K_2O	0.12	0.12	0.10	0.10	0.11	0.12	0.10	0.11	0.08	0.10	0.08	0.43	0.36	0.42
P_2O_5	0.15	0.15	0.17	0.17	0.18	0.18	0.18	0.19	0.17	0.20	0.15	0.26	0.21	0.28
Total	99.09	100.10	99.57	99.72	99.40	99.87	99.77	99.24	99.04	98.98	99.66	99.34	98.99	99.20
Mg#	59.61	55.80	59.14	58.94	57.60	57.99	57.49	58.22	57.87	58.11	65.17	61.83	60.84	61.77

	R54-4	R54-5	R54-6	R54-7	R54-8	R54-9	R54-10	R54-11	R54-12	R55SG	R56-1	R56-2	R56-3	R56-4
SiO_2	50.42	50.16	50.50	50.54	50.28	49.86	50.57	50.57	50.68	50.09	50.18	49.82	50.35	50.10
TiO_2	1.60	1.61	1.61	1.62	1.64	1.56	1.65	1.62	1.62	1.72	1.41	1.31	1.28	1.28
Al_2O_3	15.56	15.59	15.60	15.69	15.56	15.62	15.70	15.67	15.81	14.58	15.11	15.34	15.44	15.33
FeO	9.03	8.92	8.89	9.03	9.15	8.96	9.04	9.04	9.11	10.66	9.75	9.10	9.21	9.07
MnO	0.17	0.18	0.16	0.18	0.17	0.17	0.18	0.17	0.17	na	0.19	0.17	na	0.15
MgO	7.42	7.35	7.43	7.40	7.26	7.48	7.45	7.49	7.10	7.35	7.71	8.23	8.23	8.10
CaO	11.66	11.63	11.62	11.67	11.70	11.51	11.67	11.68	11.84	11.67	11.78	12.06	12.21	12.00
Na_2O	2.77	2.72	2.76	2.81	2.80	2.80	2.74	2.77	2.77	2.68	2.49	2.31	2.40	2.40
K_2O	0.43	0.45	0.45	0.44	0.44	0.42	0.41	0.42	0.45	0.10	0.09	0.08	0.09	0.09
P_2O_5	0.25	0.26	0.23	0.27	0.23	0.29	0.29	0.26	0.24	0.18	0.16	0.12	0.14	0.13
Total	99.29	98.87	99.27	99.65	99.25	98.67	99.71	99.69	99.81	99.03	98.87	98.55	99.35	98.66
Mg#	61.95	62.03	62.36	61.89	61.12	62.32	62.01	62.14	60.71	57.73	61.04	64.16	63.90	63.90

	R56-5	R56-6	R57-1	R57-2	R57-4	R57-6	R58-1	R58-2	R58-3	R58-4	R59-1	R59-3	R59-4
SiO_2	49.99	50.20	50.29	50.50	50.31	50.65	50.05	50.18	49.70	50.18	50.16	50.86	50.57
TiO_2	1.29	1.28	1.25	1.51	1.49	1.53	1.63	1.51	1.52	1.53	1.75	1.75	1.76
Al_2O_3	15.28	15.33	15.48	14.96	15.02	15.15	15.28	15.35	15.36	15.09	14.58	14.69	14.66
FeO	9.41	9.07	9.08	9.69	9.58	9.88	9.94	9.63	9.64	9.75	10.77	10.34	10.81
MnO	na	0.18	0.20	0.18	0.16	na	na	0.19	0.24	0.19	na	0.20	0.20
MgO	8.20	8.10	8.06	7.65	7.64	7.85	7.72	7.79	7.70	7.70	7.10	7.10	7.02
CaO	12.36	12.00	12.02	11.65	11.96	11.95	11.77	11.61	11.56	11.42	11.59	11.68	11.72

TABLE 4*a*. (continued)

	R56-5	R56-6	R57-1	R57-2	R57-4	R57-6	R58-1	R58-2	R58-3	R58-4	R59-1	R59-3	R59-4
Na_2O	2.39	2.40	2.42	2.51	2.51	2.54	2.48	2.54	2.56	2.51	2.63	2.62	2.69
K_2O	0.09	0.09	0.08	0.10	0.10	0.08	0.09	0.10	0.10	0.10	0.12	0.11	0.12
P_2O_5	0.15	0.14	0.16	0.16	0.16	0.18	0.17	0.17	0.17	0.19	0.19	0.19	0.17
Total	99.16	98.79	99.05	98.92	98.93	99.81	99.13	99.09	98.57	98.66	98.89	99.54	99.72
Mg#	63.32	63.90	63.73	61.00	61.23	61.15	60.60	61.57	61.27	61.01	56.63	57.63	56.26

Values are in weight percent. Samples without MnO were analyzed at the Smithsonian Institution, Washington, D. C. (T. O'Hearn analyst). Others were analyzed at University of Hawaii by Y. Niu. Group means (not listed) are computed by averaging together analyses of individual glass samples from the same dredge, provided they are similar within analytical uncertainty for all elements. For most dredges, the group means are simple averages of the individual glass analyses; however, some dredges have two groups of samples as follows: R47a: R47-1,2,3,4,5; R47b: R47-6; R49a: R49-1,2; R49b: R49-3,4; R51a: R51-3,4,5,6,7,8,9,10,11,12,13,14,15,16; R51b: R51-1,2; R56a: R56-2,3,4,5,6; R56b: R56-1; R57a: R57-2,4,6; R57b: R57-1. In this study, we have corrected U. Hawaii and Lamont probe glass data to conform with Smithsonian analyses. To do this, we multiply each oxide by the factors given in Table 4b. Complete results of the interlaboratory comparison are available from the authors and from C. Langmuir (LDGO) or J. Bender (UNCC). The probe mount of 16 glasses is kept at LDGO. $Mg^{\#}$ is Mg number, 100 x Mg/(Mg + Fe^{2+}) with $Fe^{2+}/(Fe^{2+} + Fe^{3+}) = 0.9$.

TABLE 4*b*. Correction Factors for Oxide Analyses

	SiO_2	TiO_2	Al_2O_3	FeO	MnO	MgO	CaO	Na_2O	K_2O	P_2O_5
University of Hawaii	0.9994	1.0005	1.0040	0.9737	-	1.0000	0.9792	0.9996	1.0355	1.2597
LDGO	1.0064	1.0006	1.0057	1.0062	-	0.9323	0.9876	1.0037	1.0870	1.0377

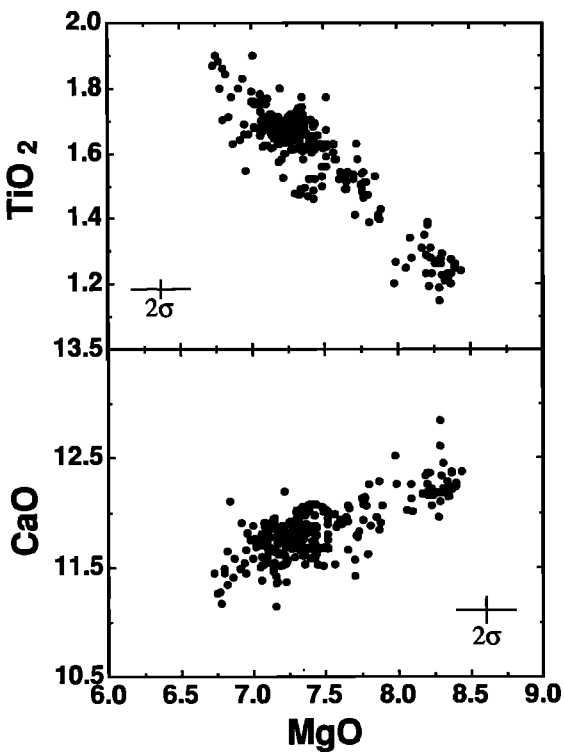

Fig. 7. Plots of TiO_2 and CaO versus MgO for all the individual glass analyses in the 9°30'N area. This plot includes data from the new axial RAITT 02 dredges, the CHEPR dredges, and the ALVIN samples.

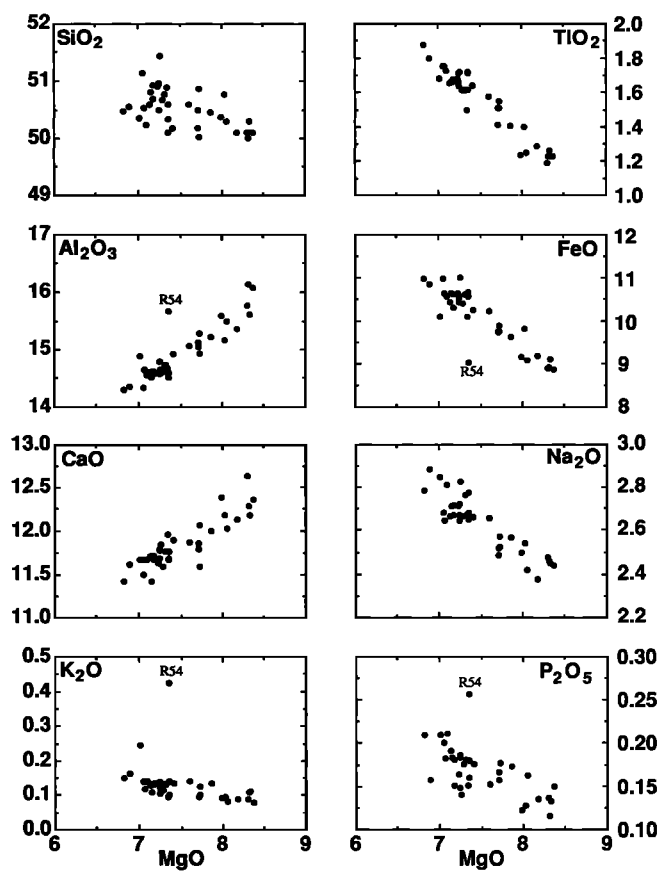

Fig. 8. MgO variation diagrams for the group means (see Table 4 notes). The E-MORB (R54) is labeled on some of the plots.

0.70252) which is within analytical error. In contrast, the E-MORB from dredge R54 is significantly higher (0.70264). Results of U-Th disequilibrium dating and ^{226}Ra-^{230}Th-Ba dating will likewise be presented elsewhere. *Volpe and Goldstein* [1990] presented preliminary results indicating that N-MORB from 9°30'N area are significantly younger (~ 2700-3000 years) than the E-MORB samples (~ 6500 years). These data, though preliminary, indicate that the E-MORB samples from 9°35'N are not related temporally to the vast majority of N-MORB erupted along this portion of the EPR.

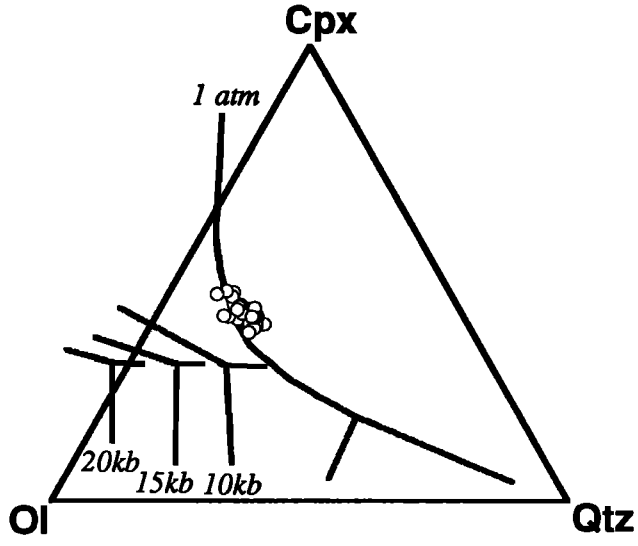

Fig. 9. Phase diagram (Cpx-Ol-Qtz) projected from plagioclase with 1-atmosphere phase boundaries from *Walker et al.* [1979] and high-pressure phase boundaries from [*Stolper*, 1980]. Note that the 9°30'N samples exhibit a very small range and plot close to the 1-atm three-phase cotectic.

INTERPRETATION AND DISCUSSIONS

Petrogenesis of N-MORB

Data presented earlier suggest that the 9°30'N N-MORB suite may be related by fractional crystallization, so we have quantitatively modeled this process. Several hundred models were tested [*Bryan*, 1986], which essentially tested the derivation of each lower-MgO liquid from each higher-MgO liquid (group means). All models considered yield very good fits (residual < 0.1) using reasonable phenocryst assemblages. A series of representative fractionation models is illustrated in Figure 13 (and Table 6) showing that the most fractionated liquids can be derived successively by fractional crystallization of the more MgO-rich melts. We emphasize that all the N-MORB melts in the 9°30'N area can be related in this manner, not only those shown in Figure 13.

A summary of the calculated models is shown in Figure 14. The phase proportions of olivine, plagioclase and cpx do not vary in this temperature interval and even the most primitive, highest temperature liquids (Mg number ≈ 65) are multiply saturated in all three phases, in agreement with the liquid-line-of-descent model of *Weaver and Langmuir* [1990] (Figure 15) and normative mineralogy of the glasses (Figure 9). In a later section, we consider the question of why, if the fractionation model fits so well, are large cpx and olivine phenocrysts virtually absent from the suite of lavas.

Figure 16 shows that trace element abundances in the lavas are consistent with the fractionation model. Only a few elements, mostly in fractionated samples, fail to match the model within analytical uncertainty. Overall, the fit of major and trace element data to the model calculations is good and is consistent with isotopic data. But could some other processes also be involved which could lead to sporadic poor fits to the trace elements?

In order to test this notion further, we have carefully evaluated mixing models using both major and trace element data. In general, the fits of mixing models to the data are no better, and in many cases are much worse, than the fractionation models. We thus cannot preclude limited mixing, however fractional crystallization is apparently the dominant process at work in the 9°30'N area, as in the area north of the Clipperton transform [*Thompson et al.*, 1989]. Trace element ratios, like trace element abundances, are in general explained within analytical uncertainties by the fractionation models. A few exceptions involving only La and Ce are shown in Figure 17. Inconsistently, one or more samples exhibit trace element ratios outside the range predicted by our simple fractionation model. This is interesting, and suggests that some additional process(es) may be involved in the petrogenesis of lavas. This process clearly does not have a large effect, as most trace element ratios even for La and Ce are predicted within error by the model. Further, this process does not affect the same samples in a consistent manner, nor are individual samples affected for all geochemically coherent elements. In addition, this process does not lead to systematic enrichment or depletion relative to the fractionation model. Thus we are at a loss to convincingly explain the origin of these minor inconsistencies. Many processes such as mantle heterogeneity, selective contamination, vapor transport, and others could be involved; however, there is no independent evidence nor convincing consistency with other data for any of these processes. Indeed, the major and trace element data plus isotope ratios are, with the few exceptions noted, well explained by a simple model of cooling and fractional crystallization from a single parent magma.

Using the chemical data presented earlier, we have tried to determine whether a single parental magma could give rise, by fractionation, to the entire 9°30'N suite of N-MORB or whether, alternatively, more than one parent is required. Within analytical uncertainties, and given the nonuniqueness of fractionation models, only one parental composition is required. In any case, if multiple parental liquids exist along the EPR axis between 9°20'N and 9°51'N, they are chemically very similar. The simplest hypothesis is that only a single parental liquid was injected to feed this entire ~ 60 km segment of the EPR.

As for the origin of this parental liquid, it could be derived from the type of aggregate primary melt proposed by *Klein and Langmuir* [1987], *McKenzie and Bickle* [1988], and *Niu and Batiza* [1991*b*]. If so, using the method of *Niu and Batiza* [1991*b*] indicates that it could be derived by column melting initiated at ~ 19 kbar (~60 km) and 1395°C and ending at ~ 12 kb (~ 40 km) and 1360°C. This aggregate melt represents about 18.5% percent melting of a mantle source such as MPY-90 [*Falloon and Green*, 1987].

Petrogenesis of E-MORB

The E-MORB at ~ 9°35'N appears to be temporally unrelated to the N-MORB suite. Because of isotopic and chemical differences it cannot be related to the N-MORB by a simple process. Clearly, if the E-MORB is derived by simple melting of the same mantle that yielded the N-MORB, it must be a very tiny fraction of melt. However, the isotopic ratios preclude this simple scenario. Like E-MORB on seamounts near the axis of the EPR [*Batiza and Vanko*, 1984; *Zindler et al.*, 1984; *Graham et al.*, 1988], the E-MORB could be a mix of an enriched mantle plum [*Hanson*, 1977] with more depleted mantle matrix.

Alternatively, a volatile-rich, tiny melt fraction of the type suggested by *Hunter and McKenzie* [1989] might be involved. The E-MORB lavas are highly vesicular (up to ~ 10% in

TABLE 5. Trace Element Chemistry of Representative Glasses

	R37-1	R38-1	R39-1	R41-1	R42-1	R44-6	R46-2	R47-3	R48-1	R49-4	R51-1	R50-1	R52-1	R54-2	R56-5	R57-6	R58-1	R59-1
La	3.54	3.86	3.83	4.29	3.61	3.92	4.08	3.52	3.76	3.83	2.50	2.94	3.68	8.40	2.75	3.38	3.37	3.95
Ce	10.70	11.90	11.50	13.70	10.40	11.90	11.60	10.00	11.40	11.60	7.70	8.50	11.70	18.90	8.50	10.60	10.50	11.80
Sm	3.71	4.04	3.67	3.91	3.33	3.70	3.69	3.27	3.70	3.75	2.84	2.84	3.73	3.80	2.93	3.36	3.61	3.96
Eu	1.33	1.41	1.32	1.39	1.21	1.33	1.35	1.20	1.33	1.31	1.07	1.07	1.37	1.36	1.07	1.20	1.26	1.41
Tb	0.91	0.95	0.92	0.92	0.84	0.89	0.94	0.77	0.94	0.90	0.71	0.66	0.96	0.82	0.69	0.78	0.88	0.94
Yb	3.41	3.74	3.42	3.50	3.07	3.48	3.55	3.10	3.56	3.51	2.71	2.64	3.58	2.96	2.76	3.18	3.35	3.75
Lu	0.501	0.565	0.488	0.506	0.445	0.514	0.507	0.429	0.500	0.513	0.385	0.394	0.504	0.412	0.405	0.458	0.487	0.540
FeO	10.72	10.87	10.28	10.53	9.91	10.44	10.66	9.88	10.35	10.47	9.12	9.04	10.56	9.05	9.17	9.81	9.95	10.86
Na_2O	2.78	2.75	2.68	2.92	2.64	2.70	2.79	2.66	2.68	2.75	2.60	2.57	2.72	2.86	2.45	2.60	2.66	2.75
Sc	43.8	43.7	42.8	44.5	42.9	43.1	44.2	43.0	42.9	43.5	40.9	39.5	42.7	41.3	39.8	41.3	39.6	43.4
Cr	177	160	313	210	293	226	251	325	233	234	345	353	264	311	344	304	301	235
Co	44.7	43.8	43.4	43.4	43.9	43.1	44.6	44.3	42.9	43.5	43.3	43.7	44.3	40.8	43.3	43.4	43.7	44.0
Ni			70	100	80	80		80	70	70	100	140	110		120	80	140	
Cs							0.21							0.15				
Sr	100	160	130	160	170	100	160	160	170	130	70	160	140	210	180	120	120	120
Ba														61				
Zr	90		150	130	150	120	120		90	150	80	110	130	130		100	110	130
Ta	0.17	0.20	0.19	0.20	0.20	0.14	0.16	0.16	0.16	0.19	0.14	0.13	0.16	0.74	0.11	0.15	0.15	0.11
Hf	2.84	3.01	2.84	2.94	2.49	2.98	2.95	2.47	2.84	2.97	2.11	2.13	2.86	2.91	2.16	2.58	2.68	3.11
Th	0.09	0.19	0.14	0.14	0.14	0.22	0.13	0.08	0.19	0.13	0.13	0.09	0.11	0.67	0.11	0.16	0.16	0.10
U														0.26				
$(La/Sm)_N$	0.668	0.669	0.731	0.768	0.759	0.742	0.774	0.754	0.711	0.715	0.616	0.725	0.691	1.547	0.657	0.704	0.653	0.698
$(La/Lu)_N$	0.730	0.706	0.811	0.876	0.838	0.788	0.832	0.848	0.777	0.771	0.671	0.771	0.754	2.107	0.702	0.763	0.715	0.756
$(Ce/Yb)_N$	0.635	0.644	0.681	0.792	0.686	0.692	0.661	0.653	0.648	0.669	0.575	0.652	0.661	1.292	0.623	0.675	0.634	0.637
Mg#	56.77	55.96	59.50	56.84	60.32	57.27	56.67	61.62	57.92	57.96	63.28	64.09	57.60	60.84	63.32	61.15	60.60	56.63

Trace elements (in ppm) were obtained by instrumental neutron activation analysis at Washington University, St. Louis, Missouri [Lindstrom and Korotev, 1982]. Analytical precision is computed for each sample and these vary slightly. Typical uncertainties (2σ) are : La and Sm, 4%; Yb, 5%; Eu and Lu, 6%; Ce, 7%; Hf, 9%; Tb, 10%; Na_2O, 0.08 wt %; FeO, 0.3 wt%; Sc, 1.2 ppm; Cr, 10 ppm; Co, 1.2 ppm; Ni, 30 ppm; Sr, 40 ppm; Zr, 50 ppm; Ba, 18 ppm; Cs, 0.07 ppm; Ta. 0.04 ppm; Th, 0.04 ppm; and U, 0.09 ppm.

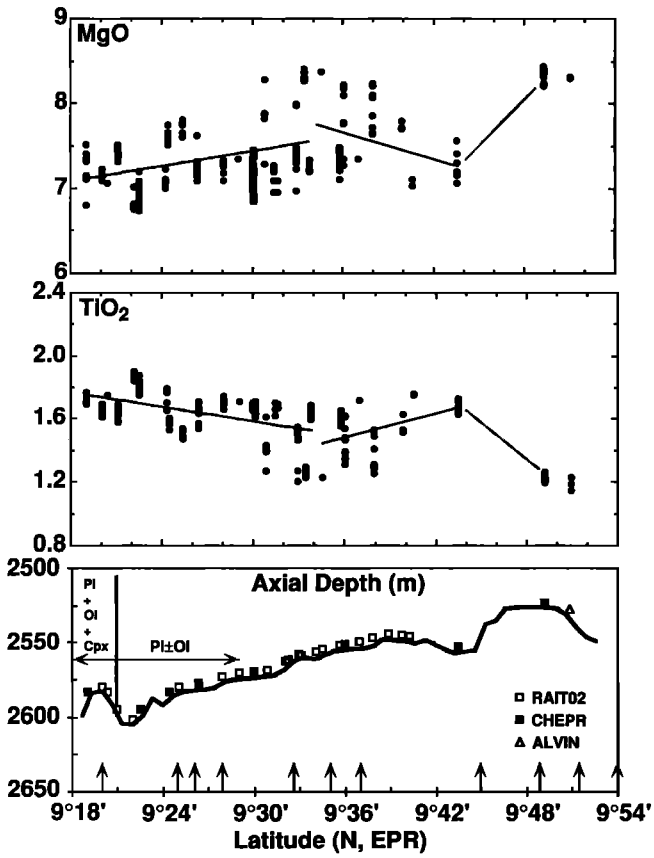

Fig. 10. Plots of MgO and TiO_2 against latitude. Circles are individual analyses. Note that local variability (scatter) is superimposed on a regular along axis trend of variation (regression lines). Regression lines are shown solid in areas of closely-spaced samples and stippled when sampling is less dense. Also shown are dredge locations, devals (arrows), topography, and petrographic observations from the 9°30'N lava suite. Note the rough correlation between average lava chemistry and topography. Comparison with Figure 1 shows that depth to the AMC also correlates with chemistry and topography. For interpretations of this correlation, see text discussions.

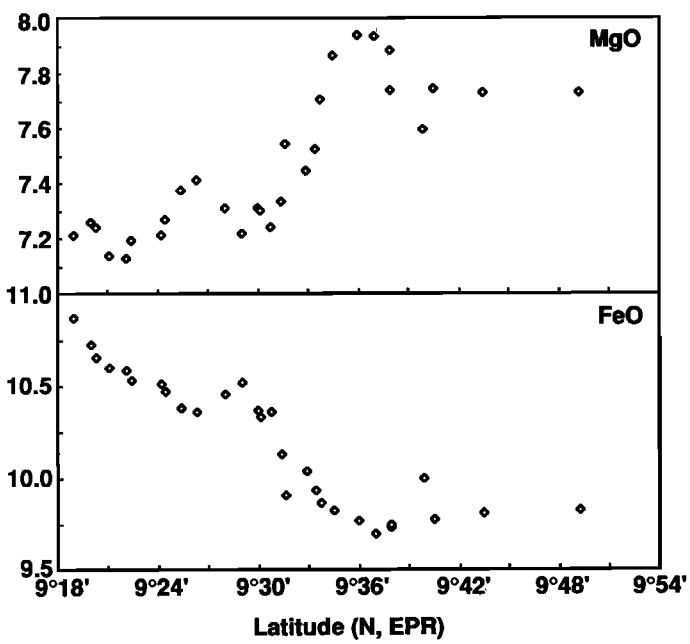

Fig. 11. The data of Figure 10 (FeO instead of TiO_2 is used here) after smoothing with a moving boxcar five dredges in width like that used by *Niu and Batiza* [1991*b*]. The regression lines in Figure 10 and the smoothed data shown here both indicate that local scatter is superimposed on a trend of regular along-axis variation.

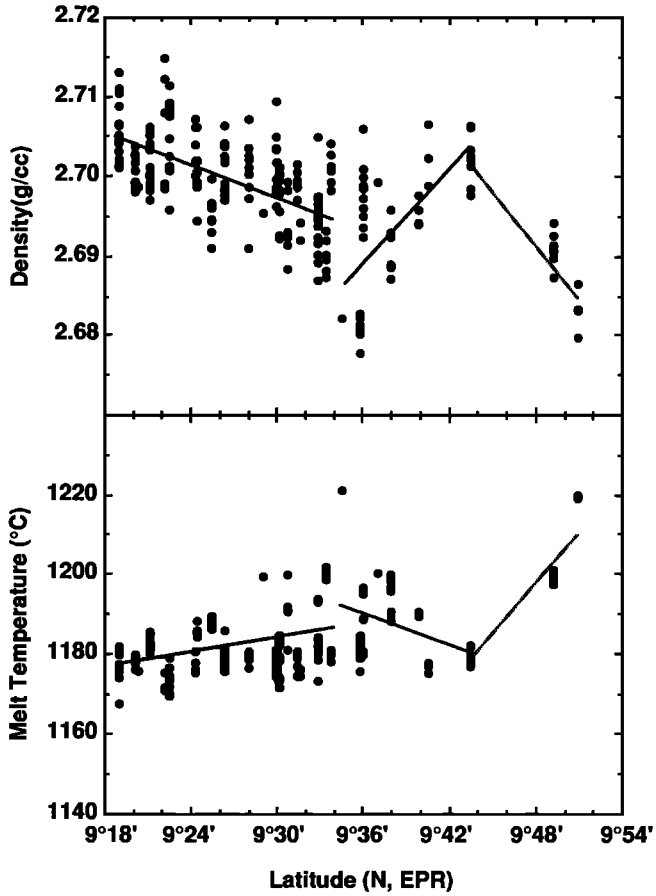

Fig. 12. Calculated density [*Niu and Batiza*, 1991*a*] and eruption temperature calculated using the data of *Bender et al.* [1984] for the 9°30'N lavas. Note that both correlate with topography (Figure 10). The least dense, highest temperature melts are erupted at local topographic highs, whereas the denser, Fe-rich melts are erupted at topographic lows where the AMC is also deepest (Figure 1).

patches) and richer in plagioclase phenocrysts than the N-MORB, perhaps consistent with this notion. On the other hand, we cannot preclude a shallow origin of the E-MORB, as assimilation or in situ crystallization [*Langmuir*, 1989; *Hekinian and Walker*, 1987] can also explain some features of the chemistry of the E-MORBs. Interestingly, the E-MORBs are the least dense melts within the 9°30'N area (Figure 18), even ignoring volatiles.

E-MORB is relatively rare in the 9°30'N area [*Perfit et al.*, 1991] and the 10°-11°N area of the EPR [*Thompson et al.*, 1989]. In contrast, it is much more abundant in the 12°-13°N of the EPR [*Hekinian et al.*, 1989]. Following the hypothesis of *Hekinian et al.* [1989], it is possible that the 9°30'N E-MORB are relict from a prior E-MORB-dominated stage of activity, now complete at 9°30'N. Their model involves episodic melting, but time variation in the processes of deep magma transport and lateral melt focusing might also produce the same results.

TABLE 6. Representative Fractionation Model Results

Parent (R53SG)	+	Olivine	+	Plagioclase	+	Clinopyroxene†	=	Daughters	Σxtl	Residuals
1.1679		-0.0258(Fo85.0)		-0.1076(An78.0)		-0.0291(Wo45.6En42.5Fs11.9)		CH89b	-0.1625	0.0124
1.2617		-0.0369(Fo85.0)		-0.1536(An77.0)		-0.0709(Wo43.1En42.9Fs12.4)		CH86	-0.2614	0.0372
1.3379		-0.0543(Fo84.4)		-0.2027(An76.0)		-0.0846(Wo42.3En34.6Fs23.1)		CH88	-0.3416	0.0213
1.4415		-0.0661(Fo84.0)		-0.2607(An75.0)		-0.1243(Wo42.3En34.6Fs23.1)		R40	-0.4511	0.0976

Olivine and plagioclase compositions are from Tables 2 and 3 respectively.
† Compositions taken from Allan et al. [1989] with similar host melt compositions.

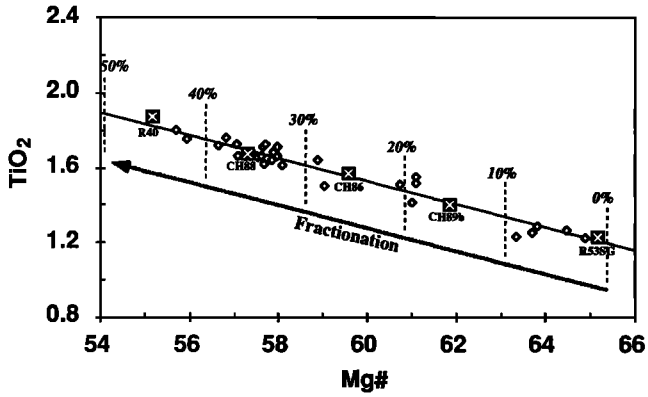

Fig. 13. Plot of TiO_2 versus $Mg/(Mg+Fe^{2+})$ for the chemical group means of the 9°30'N area to illustrate our fractional crystallization model (Table 6). Additional models tested connect all the group means and consistently yield good fits for reasonable solid assemblages.

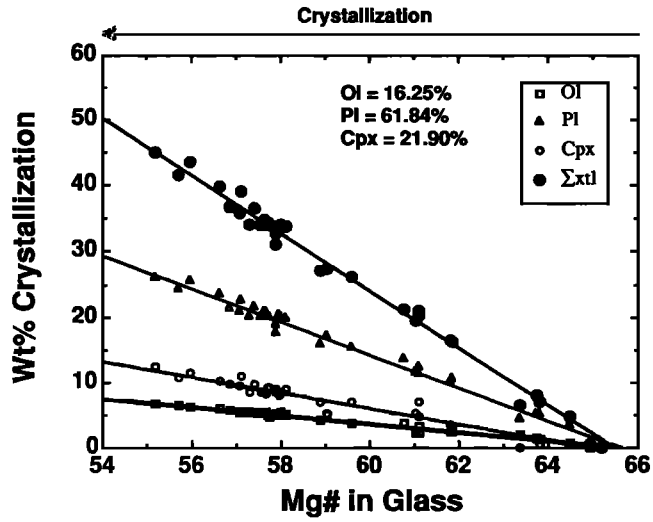

Fig. 14. Summary of the fractionation models we calculated. Note that in this range of temperature, the calculated phase proportions of the solid removed are essentially constant.

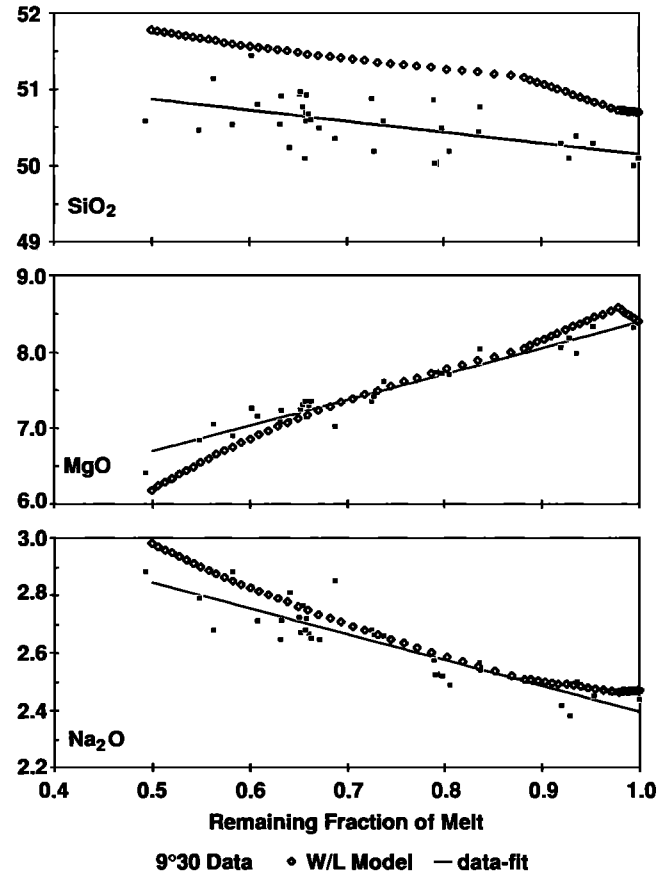

Fig. 15. Plots of SiO_2, MgO, and Na_2O versus calculated fraction of liquid remaining. These plots compare data (solid squares), our fractional crystallization model (thin solid line), and liquids predicted by the liquid-line-of-descent model (open diamonds) of *Weaver and Langmuir* [1990]. The offset in SiO_2 is due to a normalization procedure in the Weaver and Langmuir model. Note that data, our fractional crystallization model, and the liquid-line-of-descent model all agree reasonably well. This agreement is reasonable for all elements, not just the ones shown here.

Where Are the Missing Olivine and Clinopyroxene?

Although fractional crystallization models, normative mineralogy, and liquid-line-of-descent models all predict that the N-MORBs should be multiply saturated with olivine, plagioclase and cpx, most of the lavas carry phenocrysts of only plagioclase. We propose that most of the lavas have suffered solid-liquid fractionation and two lines of evidence support this idea. First, the crystal size distribution data for plagioclase suggests a pattern that has been disturbed by the addition of plagioclase crystals (> 0.5 mm in size). Second, the calculated densities of N-MORB liquids and phenocrysts (Figure 19) indicate that plagioclase should float and mafic crystals should sink in the N-MORB melts. The consistent indication is that the 9°30'N lavas represent fractionated melts with some plagioclase added and mafic phenocrysts removed by some process. Most likely this process is gravitational, though flow differentiation cannot be ruled out.

It is of interest to attempt to determine where in the magma pluming system this solid-liquid fractionation took place,

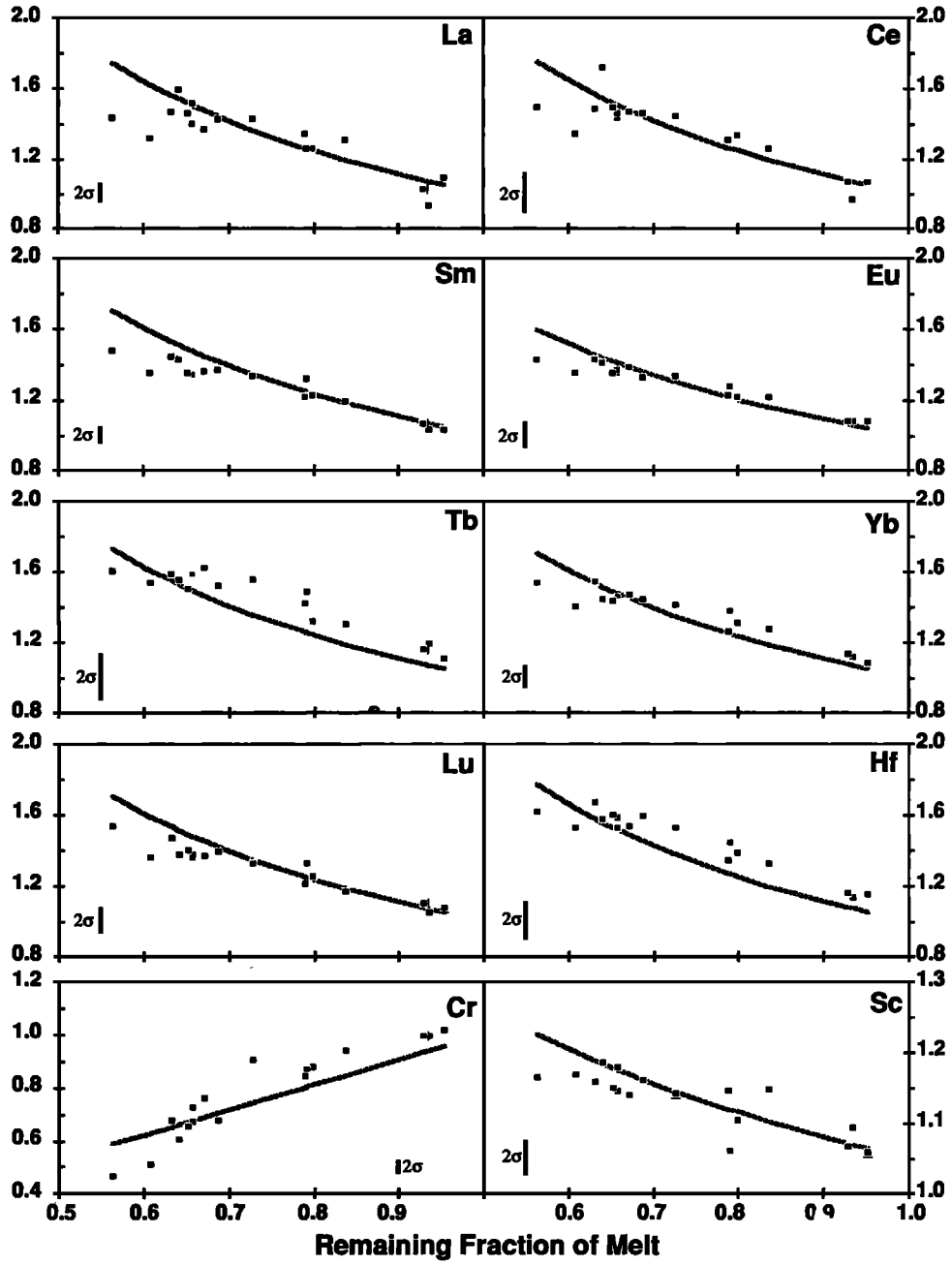

Fig. 16. Selected trace elements (Table 5) plotted to test the fractional crystallization model. The plots are all of enrichment factor ($^{Cl}/_{Co}$) versus remaining melt fraction predicted by the major element model (Figures 13 and 14). Partition coefficients used are from *McKay* [1989] for rare earth elements and *Henderson* [1982] for Hf, Sc, and Cr. The lines are the model predictions for Rayleigh fractionation (perfect fractional crystallization). Analytical error bars are plotted on each panel. Note that with very few exceptions, the data and model are in good agreement.

since this would provide clues on residence times and possibly rates of flux through the various reservoirs in the system. Clearly, solid-liquid separation could occur below the AMC or in the AMC [e.g., *Sinton and Detrick*, 1992], however, it is also possible that cooling, crystallization, and solid-liquid fractionation could occur in dikes and/or after eruption.

The latter possibility seems unlikely because if crystal settling occurred within cooling lava flows, then at least a few samples of the plagioclase-poor, olivine- and cpx-rich complement to the 9°30'N lavas should have been sampled. Collapse fractures, faulting, fissuring, and other processes at the axis prevent selective sampling of only the tops of lava flows.

In order to test whether it is plausible that the fractionation processes occurred in dikes, we consider possible cooling times of basalt liquid rising in dikes. For cooling, crystallization, and solid-liquid fractionation to have occurred in dikes, the most primitive melts would have to cool up to 60°C (see Figure 12). For a dike 1 m wide, rising in crust buffered by a hydrothermal convective geotherm (~ 400°C), this amount of cooling would require of the order of 12 hours [*Jaeger*, 1968, p. 508]. However, crystal settling in a dike 1

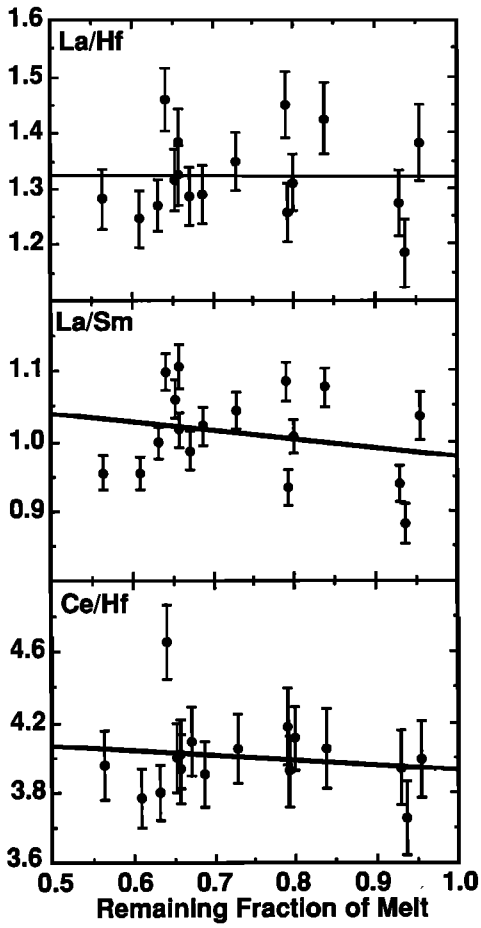

Fig. 17. Most trace element ratios agree within error [propagated as per Le Maitre [1982]) with the fractional crystallization model. Some rare examples of disagreement between the model (solid line) and the data are shown here. Note the lack of consistency in the mismatches. See text for discussion of possible interpretations.

km long or more would require several orders of magnitude longer [e.g. *Kerr and Lister*, 1991] by which time the dike would be fully solidified. This simple calculation indicate that dikes are unlikely loci for extensive cooling, fractionation and crystal settling.

These arguments tend to favor the AMC as the most likely place for solid-liquid fractionation to occur. If melt zones (or liquid-rich mush zones) are small, as seems likely [*Kent et al.*, 1990; *Sinton and Detrick*, 1992], settling distances would be relatively short (< 100 m?) and the process could occur relatively rapidly. A complication is that the large plagioclase crystals we infer to be of cumulate origin represent only a small fraction of the total plagioclase which we infer from the modeling must have crystallized from the fractionated melts. This indicates that conditions of crystallization and solid-liquid fractionation in the AMC melt-mush are probably quite complex. Crystallization in the melt lens versus surrounding mush zones may be quite different, both physically and chemically. The higher crystal content, plus the presence of cpx megacrysts in lavas south of 9°17'N where the AMC reflector is off axis, provide evidence that a crystal-rich mush zone surrounds the small AMC melt lens, as proposed by *Sinton and Detrick* [1992].

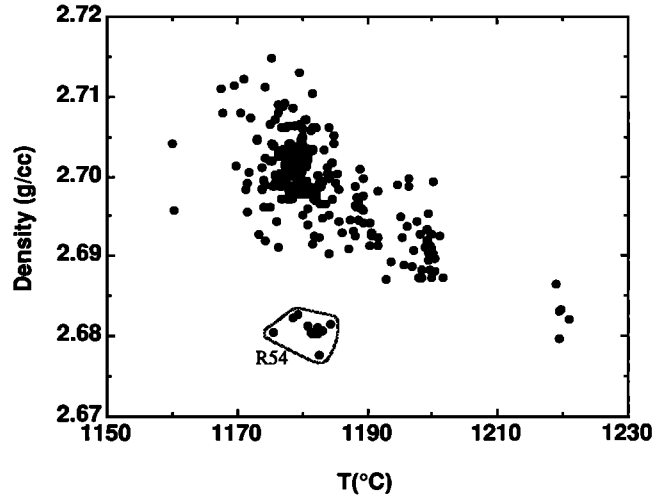

Fig. 18. Calculated volatile-free density and temperature for the 9°30'N magmas (see caption to Figure 11 for methods used). This plot illustrates the fact that the E-MORB magmas are the least dense of the low temperature liquids and thus are highly eruptable.

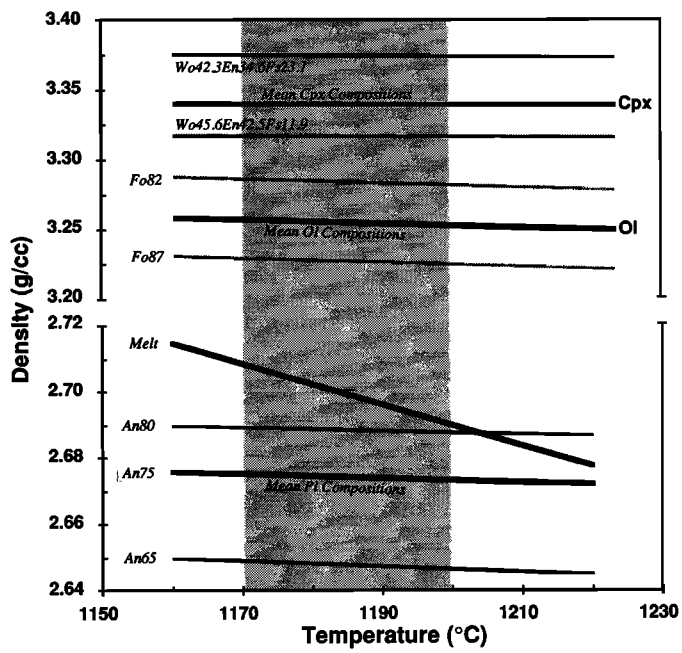

Fig. 19. Calculated densities of 9°30'N melts and solid phases [*Niu and Batiza*, 1991*a*] showing that plagioclase should float in most melts (shaded area) and olivine and cpx should sink. Note the broken density scale.

Along-Axis Chemical Variation

We now return to consider the possible causes for along-axis chemical variation within the 9°30'N area. We wish to explain not only the along-axis variation (Figure 11) but also the observed scatter that is superimposed (Figure 10). Evidently, both effects are the result of shallow-level fractional crystallization which occurred principally in the AMC melt zone, not the surrounding zone of mush. This assumes, of course, that the lavas we sampled were erupted from an AMC of roughly the same depth, extent and geometry as presently

observed. We first consider the along axis chemical variation which correlates roughly with variations in AMC depth and topography (Figures 1, 10 and 11).

If the AMC occupies a level of neutral buoyancy along axis, which seems very likely [*Ryan*, 1987], then simple extreme possibilities are (1) that the crustal lid has along-axis differences in density structure (and the melt has constant density) or (2) that the melt varies in density and composition (and the lid has a constant density gradient with depth) as shown in Figure 20. For these cases, if the axial basalts were erupted from a chamber of the present depth configuration, the along-axis chemical differences arise either because the AMC is chemically zoned along axis, or because the extent of fractionation is proportional to the lid thickness. The latter is reasonable since the amount of cooling that the melt will undergo in dikes is proportional to the distance between the top of the AMC and the surface for constant ascent rate. However, crystallization accompanies cooling, and we already have argued that it is unlikely for melt-crystal fractionation to occur in dikes.

The evidence thus seems to favor a laterally zoned magma chamber. Other more complex scenarios are also possible, of course. However, if the assumption that the axial basalts erupted from an AMC of the present extent and depth is correct, a laterally zoned chamber is the simplest interpretation. If so, then the age of the N-MORBs (~ 2700-3000 years [*Volpe and Goldstein*, 1990]) implies an AMC which is in steady state on the time scale of ~ 3000 years. Figure 21 shows the scenario we favor on the basis of data and arguments presented above. Eruptions from a zoned chamber could also explain small scale topographic changes, as the least dense melts (Figure 12) are

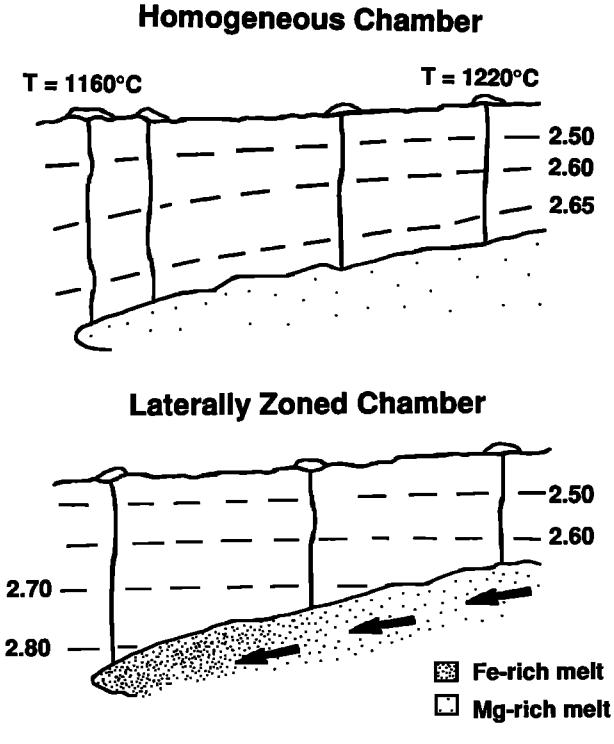

Fig. 20. Cartoon view of two extreme scenarios that result from the assumption that the AMC occupies a level of neutral buoyancy. We favor the interpretation in the lower panel because of the observed along-axis variation in chemistry and because it is unlikely that chemical differentiation could arise from processes occurring in dikes or in flows after eruption.

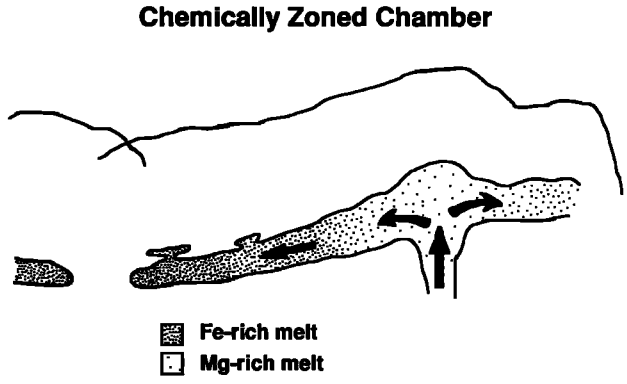

Fig. 21. Cartoon view of the scenario we favor to explain the along-axis chemical variation in the 9°30'N area. This shows a chemically zoned magma lens with small, semiisolated pockets of melt to explain the local chemical variation observed at any place along the axis (scatter).

located at the highest portion of the axis, as predicted by simple magma-static head arguments.

While an AMC that is chemically zoned along axis seems to adequately explain the along-axis variation, it does not provide a simple explanation for the observed local scatter (Figure 10). If the chamber were chemically stratified, then individual eruptions from the AMC could vary chemically, but if the AMC is very small [*Kent et al.*, 1990; *Sinton and Detrick*, 1992] chemical stratification seems unlikely. However, small scale along-axis segmentation of the AMC, with small semiisolated pockets of melt which cool at slightly different rate, could explain the observed scatter. Small-scale temporal variation caused by the dynamic processes of AMC recharge could enhance local variation at any spot along the EPR axis.

AMC Resupply Dynamics

If a laterally zoned magma chamber is present below the 9°30'N area of the EPR, it is of interest to ask how it achieved its chemically zoned state. One possibility is that when it was first emplaced it was homogeneous and that simple cooling has resulted in chemical zonation. However, this seems unlikely, as the deepest portions of the chamber (most Fe-rich) would have to cool the most. This would require large lateral gradients in thermal structure for which there is no evidence. Another possibility is that the chamber was emplaced in a zoned configuration by vertical ascent of magma from below. This also is possible but requires that the observed fractionation occur during this deeper ascent prior to emplacement. Petrological evidence presented earlier makes this unlikely.

Another possibility is that the chamber acquired its zonation during emplacement or resupply. If we consider a central injection model of the type suggested by *Sempere and Macdonald* [1986] and *Macdonald et al.* [1988], which is similar to models of magmatic pluming below Icelandic and Hawaiian rift zones, then very slow along-axis emplacement of an AMC could cause chemical zonation. In this model of very slow emplacement, the earliest magma emplaced would travel along axis the farthest from the initial site of vertical injection and consequently would cool the most. However, for a small AMC, the emplacement time in this model would have to be a significant fraction of the life of the AMC itself. This fraction is essentially the time needed for the magma to cool ~ 60°C

balanced against the time needed for complete solidification (cooling of 100°-200°C [*Yoder*, 1976]). For this reason, a very slow along-axis injection model seems unlikely.

An alternative to slow injection is episodic central recharge of the AMC. This model also could produce a zoned chamber if new melt batches have a higher probability of being injected only a short distance along axis [*Macdonald et al.*, 1987]. Lateral mixing by convection in a long chamber with a small cross section is thought to be negligible [*Oldenberg et al.*, 1989; *Sinton and Detrick*, 1992], so, if new melt batches are injected only limited distances along axis and do not reach the distal ends, older fractionated magma could be preserved even with frequent episodes of lateral resupply. If this occurred in the 9°30'N area, all the melt batches supplied episodically would have to be identical or nearly identical chemically and isotopically.

Implications for Magma Supply at the EPR

Our interpretations of the data presented above favor a chemically zoned AMC beneath 9°30'N. We favor a melt zone or lens of the type suggested by *Kent et al.* [1990] and *Sinton and Detrick* [1992]. A long, narrow, and laterally restricted melt lens can explain most of the features we observe. If the melt lens is segmented [*Toomey et al.*, 1990] and/or has a complex geometry and/or the thermal structure is heterogeneous, such a lens may simultaneously host melts of variable chemistry. This could explain the range of chemistry we see at any given site along axis. Alternatively, this variation may be the result of small age differences among the N-MORB lavas at any given site. Recent dense sampling of the 9°30N area [*Perfit et al.*, 1991] will probably be extremely helpful in distinguishing among the possibilities.

In order to create a zoned magma chamber, we favor a dynamic along-axis emplacement model like that of *Macdonald et al.* [1987, 1988], with episodic resupply of magma. Thermal models [e.g. *Wilson et al.*, 1988] suggest that chambers may come and go at any locality along the EPR. The presence of older E-MORB in the 9°30'N area is consistent with the episodic presence of the AMC because the E-MORB most likely erupted at a time when the AMC was absent or much smaller in size. Otherwise, it would have mixed with N-MORB in the AMC prior to eruption. If so, the present AMC at 9°30'N is probably younger than ~ 6500 years (the age of the E-MORB).

Our data favor an important role for the AMC in volcanic-tectonic segmentation of the EPR [*Toomey et al*, 1990]. However, since we find the same parental magma along ~ 60 km of the EPR, central injection sites must be spaced at greater intervals than the smallest scale segmentation. Deval-bounded, 4th-order segmentation may be correlated with systematic along-axis fractionation differences, but these are below the resolution of our sampling so far. Overall, our new data favor a hierarchical supply system like that proposed by *Langmuir et al.* [1986], *Macdonald et al.* [1987, 1988] and *Sinton et al.* [1991].

SUMMARY AND CONCLUSIONS

(1) The axis of the EPR in the 9°30'N area (9°17'N to 9°51'N) has mostly N-MORB with a narrow range of MgO and usually plagioclase phenocrysts only. The chemistry of the lavas varies along axis, correlating roughly with elevation of the axis and depth to the axial magma chamber (AMC). (2) Major and trace element data are best explained by derivation of all the 9°30'N N-MORB from a single parental melt by fractional crystallization of olivine, plagioclase, and clinopyroxene. (3) The virtual absence of olivine and cpx phenocrysts plus crystal size distribution analysis for plagioclase are best explained by crystal settling (olivine and cpx) and flotation (plagioclase) occurring in the AMC. However, in detail, this process is probably complex, involving melt migration from the mush zone into the melt lens. (4) Enriched E-MORB at 9°35'N is older and not directly related to the N-MORB. It probably erupted at a time when the AMC was absent or much smaller in size, perhaps at the initiation of a new magmatic cycle. (5) Along-axis chemical variation and correlation of chemistry with depth to the AMC is best explained as the results of eruptions from an AMC that is chemically zoned along its length, with Fe-rich dense melts at the distal, deep ends of the AMC. Correlation with topography may be explained by melt density with least dense melts creating higher volcanic constructions. (6) Local chemical variations at any site along the EPR at ~ 9°30'N may be due to segmentation of the AMC, small pockets of melt, heterogeneity in thermal structure, and/or small-scale temporal variation resulting from AMC resupply dynamics. (7) Chemical zonation of the AMC could result from numerous processes, but we favor a dynamic cause related to central episodic injection of MgO-rich magma at sites along the axis with lateral along-axis transport. Injection sites are apparently spaced on the order of 50 km or more and thus do not correspond to the 4th-order deval-bounded segmentation.

Acknowledgments. We are grateful to Captain Tom DeJardin and the crew of the R/V Thomas Washington for their expertise, assistance, and a memorable ceremony on the bow. We thank the scientific party on RAITT 02 for their tireless efforts, musical talents, good cheer, and companionship. We especially thank D. Vanko, J. Karsten, and R. Sack. We also thank R. Comer, M. Moore, and W. Smith for their expert assistance at sea and before and after the cruise. We are grateful to T. O'Hearn for glass analyses and to L. Haskin and R. Korotev for INAA analyses. We have benefited from conversations with many colleagues. In particular, we thank J. Sinton, A. Volpe, S. Goldstein, R. Detrick, D. Toomey, B. Marsh, D. Fornari, R. Haymon, M. Purdy, W. White, K. Harpp, E. Klein, C. Langmuir, J. Bender, M. Garcia, and M. Perfit. We thank M. Purdy and D. Toomey for kindly providing a copy of their Seabeam map collected on RAITT 01. The manuscript benefited greatly from reviews by E. Klein, M. Perfit, J. Sinton, and the comments from A. Glazner. We thank the NSF (OCE 89-96191 and OCE-90-00193) and the Office of Naval Research for support. This is SOEST contribution 2730.

REFERENCES

Allan, J. F., R. Batiza, M. R. Perfit, D. J. Fornari, and R. O. Sack, Petrology of lavas from the Lamont seamount chain and adjacent East Pacific Rise, 10°N, *J. Petrol.*, *30*, 1245-1298, 1989.

Batiza, R., and D. A. Vanko, Petrology of young Pacific seamounts, *J. Geophys. Res.*, *89*, 11,235-11,260, 1984.

Batiza, R, Y. Niu, and W. C. Zayac, Chemistry of seamounts near the East-Pacific Rise: Implications for the geometry of sub-axial mantle flow, *Geology*, *18*, 1122-1125, 1990.

Batiza, R, B. R. Rosendahl, and R. L. Fisher, Evolution of ocean crust, 3, Petrology and geochemistry of basalts from the East Pacific Rise and Siqueiros transform fault, *J. Geophys. Res.*, *82*, 265-276, 1977.

Bender, J. F., C. H. Langmuir, and G. N. Hanson, Petrogenesis of basalt glasses from the Tamayo region, East Pacific Rise, *J. Petrol.*, *25*, 213-254, 1984.

Brodholdt, J., and R. Batiza, Magma supply processes in the tomography area (~ 9°30'N) of the EPR (abstract), *Eos Trans. AGU*, 305, 1988.

Bryan, W. B., Linked evolutionary data arrays: A logical structure for petrologic modeling of multisource, multiprocess magmatic systems, *J. Geophys. Res.*, *91*, 5891-5900, 1986.

Carbotte, S., and K. C. Macdonald, East Pacific Rise 8°-10°30'N: Evolution of ridge segments and discontinuities from Sea Marc II and three-dimensional magnetic studies, *J. Geophys. Res.*, in press, 1992.

Cashman, K. V., and B. C. Marsh, Crystal size distribution (CSD) in rocks and the kinetics and dynamics of crystallization, II, Makaopuhi lava lake, *Contrib. Mineral. Petrol.*, *99*, 292-305, 1988.

Detrick, R. S., J. P. Madsen, P. E. Buhl, J. Vera, J. Mutter, J. Orcutt, and T. Brocker, Multichannel seismic imaging of an axial magma chamber along the East Pacific Rise between 4°N and 13°N, *Nature*, *326*, 35-41, 1987.

Detrick, R. S., J. C. Mutter, P. Buhl, and I. I. Kim, No evidence from multichannel reflection data for a crustal magma chamber in the MARK area of the mid-Atlantic ridge, *Nature*, *347*, 61-64, 1990.

Falloon, T. J., and D. H. Green, Anhydrous partial melting of MORB pyrolite and other peridotite compositions at 10 kbar: Implications for the origin of MORB glasses, *Mineral. Petrol.*, *37*, 181-219, 1987.

Fornari, D. J., W. B. F. Ryan, and P. J. Fox, The evolution of craters and calderas on young seamounts: Insights from Sea Marc I and Sea Beam sonar surveys of a small seamount group near the axis of the East Pacific Rise at ~ 10°N, *J. Geophys. Res.*, *89*, 11,069-11,083, 1984.

Fornari, D. J., M. R. Perfit, J. F. Allan, R. Batiza, R. Haymon, A. Barone, W. B. F. Ryan, T. Smith, T. Simkin, and M. Luckman, Geochemical and structural studies of the Lamont seamounts: Seamounts as indicators of mantle processes, *Earth Planet. Sci. Lett.*, *89*, 63-83, 1988.

Garcia, M. O., and E. W. Wolfe, Petrology of erupted lavas, in The Puu Oo eruption of Kilauea volcano, Hawaii: Episodes 1 through 20, January 3, 1983 through June 1984, edited by *U.S. Geol. Surv. Prof. Pap. 1462*, 127-148, 1988.

Garcia, M. O., F. A. Frey, and D. G. Grooms, Petrology of volcanic rocks from Kaula Island, Hawaii, *Contrib. Mineral. Petrol.*, *94*, 461-471, 1986.

Gente, P., J. M. Auzende, V. Renard, Y. Fouguet, and D. Bideau, Detailed geologic mapping by submersible of the East Pacific Rise axial graben near 13°N, *Earth Planet. Sci. Lett.*, *78*, 229-236, 1986.

Glazner, A. F., Activities of olivine and plagioclase components in silicate melts and their application to geothermometry, *Contrib. Mineral. Petrol.*, *88*, 260-268, 1984.

Graham, D. W., A. Zindler, M. D. Kurz, W.J . Jenkins, R. Batiza, and H. Staudigal, He, Pb, Sr, and Nd isotope constraints on magma genesis and mantle heterogeneity beneath young Pacific seamounts, *Contrib. Mineral. Petrol.*, *99*, 446-463, 1988.

Hanson, G. N., Geochemical evolution of the suboceanic mantle, *J. Geol. Soc. London*, *134*, 235-253, 1977.

Harding, A. J., J. Orcutt, M. Kappus, E. Vera, J. Mutter, P. Buhl, R. Detrick, and T. Brocher, The structure of young oceanic crust at 13°N on the East Pacific Rise from expanding spread profiles, *J. Geophys. Res.*, *94*, 12,163-12,196, 1989.

Harpp, K., W. M. White, and R. Batiza, Isotopic study of contrasting magmatic studies: The East Pacific Rise at 9°30/N and the MAR in the FAMOUS area (abstract), *Eos Trans. AGU*, *71*, 658, 1990.

Haymon, R., D. J. Fornari, M. H. Edwards, S. Carbotte, D. Wright, and K. C. Macdonald, Hydrothermal vent distribution along the East Pacific Rise crest (9°09' - 59'N) and its relationship to magmatic and tectonic processes on fast-spreading mid-ocean ridges, *Earth Planet. Sci. Lett.*, *104*, 513-534, 1991*a*.

Haymon, R. et al., Eruption of the EPR crest at 9°45' - 52'N since late 1989 and its effects on hydrothermal venting: Results of the ADVENTURE Program, a ODP site survey with ALVIN (abstract), *Eos Trans. AGU*, 72, 480, 1991*b*.

Hekinian, R., and D. Walker, Diversity and spatial zonation of volcanic rocks from the East Pacific Rise near 21°N, *Contrib. Mineral. Petrol.*, *96*, 265-280, 1987.

Hekinian, R., G. Thompson, and D. Bideau, Axial and off-axial heterogeneity of basaltic rocks from the East Pacific Rise at 12°35'N-12°51'N, *J. Geophys. Res.*, *94*, 17,437-17,463, 1989.

Henderson, P., Inorganic geochemistry, 353 pp, Pergamon Press, Elmsford, N. Y., 1982.

Housh, T. B., and J. F. Luhr, Plagioclase-melt equilibria in hydrous system, *Am. Mineral.*, *76*, 477-492, 1991.

Hunter, R. H., and D. P. McKenzie, the equilibrium geometry of carbonate melts in rocks of mantle composition, *Earth Planet. Sci. Lett.*, *92*, 347-356, 1989.

Jaeger, J. C., Cooling and solidification of igneous rocks, in Basalts, vol. 2, edited by H. H. Hess and A. Poldervaart, pp. 503-536, Wiley Interscience, New York, 1968.

Kent, G. M., A. J. Harding, and J. A. Orcutt, Evidence for a smaller magma chamber beneath the East Pacific Rise at 9°30'N, *Nature*, *344*, 650-653, 1990.

Kent, G. M., A. J. Harding, and J. A. Orcutt, Reprocessed CDP lines between 8°50'N and 9°50'N on the East Pacific Rise: Implications for layer 2A thickness, segmentation of the axial magma chamber and decoupling of the melt source region from the neovolcanic zone (abstract), *Eos Trans. AGU*, *72*, 490, 1991.

Kerr, R. C., and J. R. Lister, The effects of shape on crystal settling and the rheology of magmas, *J. Geol.*, *99*, 457-467, 1991.

Klein, E. M., and C. L. Langmuir, Global correlations of ocean ridge basalt chemistry with axial depth and crustal thickness, *J. Geophys. Res.*, *92*, 8089-8115, 1987.

Langmuir, C. H., Geochemical consequence of in situ crystallization, *Nature*, *340*, 199-205, 1989.

Langmuir, C. H., J. F. Bender, and R. Batiza, Petrological and tectonic segmentation of the East Pacific Rise, 5°30'-14°30', *Nature*, *322*, 422-429, 1986.

Le Maitre, R. W., Numerical Petrology, 281 pp., Elsevier Science, New York, 1982.

Lin, J., and J. Phipps Morgan, The spreading rate dependance of three-dimensional mid-ocean ridge gravity structure, *Geophys. Res. Lett.*, *19*, 13-16, 1992.

Lindstrom, D. J., and R. L. Korotev, TEABAGS: A computer program for instrumental neutron activation analysis, *J. Radioanal. Chem.*, *70*, 439-458, 1982.

Lonsdale, P., Nontransform offsets of the Pacific-Cocos plate boundary and their traces on the rise flanks, *Geol. Soc. Am., Bull.*, *96*, 313-327, 1985.

Lonsdale, P., Segmentation of the Pacific-Nazca spreading center, *J. Geophys. Res*, *94*, 12,197-12,226, 1989.

Macdonald, K. C., and P. J. Fox, The axial graben and cross-sectional shape of the East Pacific Rise as indicators of axial magma chambers and recent volcanic eruptions, *Earth Planet. Sci. Lett.*, *88*, 119-131, 1988.

Macdonald, K. C., J. -C. Sempere, and P. J. Fox, East Pacific Rise from Siqueiros to Orozco fracture zones: Along strike continuity of axial neo-volcanic zones and structure and evolution of overlapping spreading centers, *J. Geophys. Res.*, *89*, 6049-6069, 1984.

Macdonald, K. C., J. C. Sempere, P. J. Fox, and R. Tyce, Tectonic evolution of ridge axis discontinuities by the meeting, liking and self-decapitation of neighboring ridge segments, *Geology*, *15*, 993-997, 1987.

Macdonald, K. C., P. J. Fox, L. J. Perram, M. F. Eisen, R. M. Haymon, S. P. Miller, S. M. Carbotte, M. -H. Cormier, and A. N. Shor, A new view of the mid-ocean ridge from the behavior of ridge axis discontinuities, *Nature*, *335*, 217-225, 1988.

Marsh, B. D., Crystal size distribution (CSD) in rocks and the kinetics and dynamics, I, Theory, *Contrib. Mineral. Petrol.*, *99*, 277-291, 1988.

McKay, G. A., Partitioning of rare earth elements between major silicate minerals and basaltic melts, *Rev. Mineral.*, *21*, 45-78, 1989.

McKenzie, D., and M. J. Bickle, The volume and composition of melt generated by extension of the lithosphere, *J. Petrol.*, *29*, 625-679, 1988.

Mutter, J. C., G. A. Barth, P. Buhl, R. S. Detrick, J. Orcutt, and A. Harding, Magma distribution across ridge-axis discontinuities on the East Pacific Rise from multichannel seismic images, *Nature*, *336*, 156-158, 1988.

Natland, J. H., Crystal morphologies in basalt dredged and drilled from the East Pacific Rise near 9°N and the Siqueiros fracture zone, *Initial Rep. Deep Sea Drill. Proj.*, *54*, 605-634, 1980*a*.

Natland, J. H., Effects of axial magma chambers beneath spreading centers on the compositions of basaltic rocks, *Initial Rep. Deep Sea Drill. Proj.*, *54*, 833-850, 1980*b*.

Natland, J. H., Partial melting of a lithologically heterogeneous

mantle: inferences from crystallization histories of magnesian abyssal tholeiites from the Siqueiros fracture zone, in Magmatism in the Ocean Basin, edited by A. D.Saunders and M.J. Norry, *Geol. Soc. Spec. Publ., London, 42*, 41-70, 1989.

Niu, Y., and R. Batiza, DENSCAL: A program for calculating densities of silicate melts and mantle minerals in melting range, *Comput. and Geosci., 17*, 679-687, 1991*a*.

Niu, Y., and Batiza, R., An empirical method for calculating melt compositions produced beneath mid-ocean ridges: Application for axis and off-axis (seamounts) melting. *J. Geophys Res., 96*, 21,753-21,777, 1991*b*.

Oldenberg, C. M., F. J. Spear, D. A. Yuen, and G. Sewell, Dynamic mixing in magma bodies: Theory, simulations and implications, *J. Geophys. Res., 94*, 9215-9236, 1989.

Perfit, M. R., D. J. Fornari, A. Malahoff, and R. W. Embley, Geochemical studies of abyssal lavas recovered by DSRV from Eastern Galapagos Rift, Inca Transform, and Ecuador Rift, 3, Trace element abundances and petrogenesis, *J. Geophys. Res., 88*, 10,551-10,572, 1983.

Perfit, M. R., D. J. Fornari, M. Smith, C. H. Langmuir, J. Bender and R. Haymon, Fine-scale petrologic variations along the East Pacific Rise crest 9°17'N to 9°54'N: results from ALVIN diving and rock coring during the ADVENTURE Program (abstract), *Eos Trans. AGU,72*, 491, 1991.

Perram, L. J., and K. C. Macdonald, A one-million-year history of the 11°45'N East Pacific Rise discontinuity, *J. Geophys. Res., 95*, 21,363-21,381, 1990.

Roeder, P. L., and R. F. Emslie, Olivine-liquid equilibrium, *Contrib. Mineral. Petrol., 29*, 275-289, 1970.

Ryan, M. P., Neutral buoyancy and the mechanical evolution of magmatic systems, in Magmatic Processes: Physical Chemical Principles, edited by B. O. Mysen, *Geochem. Soc. Spec. Publ., 1*, 259-305, 1987.

Sempere, J. C., and K. C. Macdonald, Deep-tow studies of the overlapping spreading center at 9°30'N on the East Pacific Rise, *Tectonics*, 5, 881-900, 1986.

Sinton, J. M., and R. S. Detrick, Mid-ocean ridge magma chambers, *J. Geophys. Res., 97*, 197-216, 1992.

Sinton, J. M., S. M. Smaglik, J. J. Mahoney, and K. C. Macdonald, Magmatic processes at super fast spreading ridges: Glass compositional variations along the EPR 13° - 23°S, *J. Geophys. Res., 96*, 6133-6155, 1991.

Stolper, E., A phase diagram for mid-ocean ridge basalts: Preliminary results and implications for petrogenesis, *Contrib. Mineral. Petrol., 74*, 13-27, 1980.

Thompson, G., W. B. Bryan, and S. E. Humphris, axial volcanism on the East Pacific Rise, 10° - 12°N, in Magmatism in the Ocean Basin, edited by A. D. Saunders and M. J. Norry, *Geol. Soc. Spec. Publ., 42*, 181-200, 1989.

Tighe, S.(Ed.), East Pacific Rise data synthesis report, Joint Oceanographic Institutions, Inc., Washington, D. C., 1988.

Toomey, D. R., G. M. Purdy, S. C. Solomon, and W. S. D. Wilcock, The three-dimensional seismic velocity structure of the East Pacific Rise near latitude 9°30'N, *Nature, 347*, 639-645, 1990.

Ulmer, P., The dependence of the Fe^{2+}-Mg cation-partitioning between olivine and basaltic liquid on pressure, temperature and composition, *Contrib. Mineral. Petrol., 101*, 261-273, 1989.

Volpe, H. M., and S. J. Goldstein, Dating young MORB: ^{226}Ra-^{230}Th isotopic disequilibria measured by mass spectrometer (abstract), *Eos Trans. AGU, 71*, 1702, 1990.

Walker, D., T. Shibata, and S.E. DeLong, Abyssal tholeiites from the Oceanographer Fracture zone, II, phase equilibria and mixing, *Contrib. Mineral. Petrol., 70*, 111-125, 1979.

Weaver, J. S., and C. H. Langmuir, Calculation of phase equilibrium in mineral-melt systems, *Comput. Geosci., 16*, 1-19, 1990.

Wilson, D. S., D. A. Clague, N. H. Sleep, and J. Morton, A model for narrow, steady state magma chambers on fast spreading ridges, *J. Geophys. Res., 93*, 11,974-11,984, 1988.

Yoder, H. S., *Generation of Basaltic Magma*, 265 pp., National Academy of Science Press, Washington D. C., 1976.

Zindler, A., H. Staudigel, and R. Batiza, Isotope and trace element geochemistry of young Pacific seamounts: Implications for the scale of upper mantle heterogeneity, *Earth Planet. Sci. Lett., 70*, 175-195, 1984.

R. Batiza and Y. Niu, School of Ocean and Earth Science and Technology, University of Hawaii at Manoa, 2525 Correa Road, Honolulu, HI 96822.

**(Received July 16, 1991;
revised January 7, 1992;
accepted January 20, 1992.)**